Earth and Planetary Science Letters 494 (2018) 172–189

Contents lists available at ScienceDirect

Earth and Planetary Science Letters

www.elsevier.com/locate/epsl

Peridotites and basalts reveal broad congruence between two independent records of mantle f_{O2} despite local redox heterogeneity

Suzanne K. Birner [a,b,*], Elizabeth Cottrell [b], Jessica M. Warren [c], Katherine A. Kelley [d], Fred A. Davis [e]

[a] Department of Geological Sciences, Stanford University, 450 Serra Mall, Building 320, Stanford, CA 94305, USA
[b] National Museum of Natural History, Smithsonian Institution, Washington, DC 20560, USA
[c] Department of Geological Sciences, University of Delaware, Penny Hall, Newark, DE 19716, USA
[d] Graduate School of Oceanography, University of Rhode Island, Narragansett, RI 02882, USA
[e] Department of Earth and Environmental Sciences, University of Minnesota Duluth, 229 Heller Hall, 1114 Kirby Drive, Duluth, MN 55812, USA

ARTICLE INFO

Article history:
Received 25 October 2017
Received in revised form 30 March 2018
Accepted 18 April 2018
Available online xxxx
Editor: M. Bickle

Keywords:
oxygen fugacity
mid-ocean ridge
basalt
peridotite
upper mantle

ABSTRACT

The oxygen fugacity (f_{O2}) of the oceanic upper mantle has fundamental implications for the production of magmas and evolution of the Earth's interior and exterior. Mid-ocean ridge basalts and peridotites sample the oceanic upper mantle, and retain a record of oxygen fugacity. While f_{O2} has been calculated for mid-ocean ridge basalts worldwide (>200 locations), ridge peridotites have been comparatively less well studied (33 samples from 11 locations), and never in the same geographic location as basalts.

In order to determine whether peridotites and basalts from mid-ocean ridges record congruent information about the f_{O2} of the Earth's interior, we analyzed 31 basalts and 41 peridotites from the Oblique Segment of the Southwest Indian Ridge. By measuring basalts and peridotites from the same ridge segment, we can compare samples with maximally similar petrogenetic histories. We project the composition and oxygen fugacity of each lithology back to source conditions, and evaluate the effects of factors such as subsolidus diffusion in peridotites and fractional crystallization in basalts.

We find that, on average, basalts and peridotites from the Oblique Segment both reflect a source mantle very near the quartz–fayalite–magnetite (QFM) buffer. However, peridotites record a significantly wider range of values (nearly 3 orders of magnitude in f_{O2}), with a single dredge recording a range in f_{O2} greater than that previously reported for mid-ocean ridge peridotites worldwide. This suggests that mantle f_{O2} may be heterogeneous on relatively short length scales, and that this heterogeneity may be obscured within aggregated basalt melts. We further suggest that the global peridotite f_{O2} dataset may not provide a representative sample of average basalt-source mantle. Our study motivates further investigation of the f_{O2} recorded by ridge peridotites, as peridotites record information about the f_{O2} of the Earth's interior that cannot be gleaned from analysis of basalts alone.

1. Introduction

The oxygen fugacity (f_{O2}) of the oceanic upper mantle plays an important role in the production of melts and fluids beneath mid-ocean ridges. Oxygen fugacity affects the speciation of fluids (e.g., O'Neill and Wall, 1987; Wood et al., 1990; Frost and McCammon, 2008), the stability of many mineral phases such as oxides, sulfates/sulfides, and carbon-bearing minerals, which in turn affect the position of the mantle solidus (e.g., Dasgupta and Hirschmann, 2006; Stagno et al., 2013), and the partitioning behavior of multivalent elements such as Fe, Cr, V, C, and S (e.g., Wood et al., 1990; Canil, 1997; Frost and McCammon, 2008; Gaillard et al., 2015). In addition, uncertainty in the oxygen fugacity of sub-ridge mantle can have large implications for the calculation of important ridge parameters such as primary magma composition and the thickness of the oceanic crust (e.g., Herzberg and Asimow, 2015; Putirka, 2016). Precise constraints on the absolute value and variability of mantle f_{O2} are particularly important because small variations affect our interpretation of mantle velocity anomalies (e.g., Dalton et al., 2014), mantle potential temperature (e.g. Herzberg and Asimow, 2015), phase equilibria (e.g., Dasgupta and Hirschmann, 2006), and gas speciation (e.g., Gaillard et al., 2011).

To investigate the oxygen fugacity of sub-ridge mantle, geoscientists have primarily used two distinct proxies—the oxygen

* Corresponding author.
E-mail address: skbirner@stanford.edu (S.K. Birner).

https://doi.org/10.1016/j.epsl.2018.04.035
0012-821X/

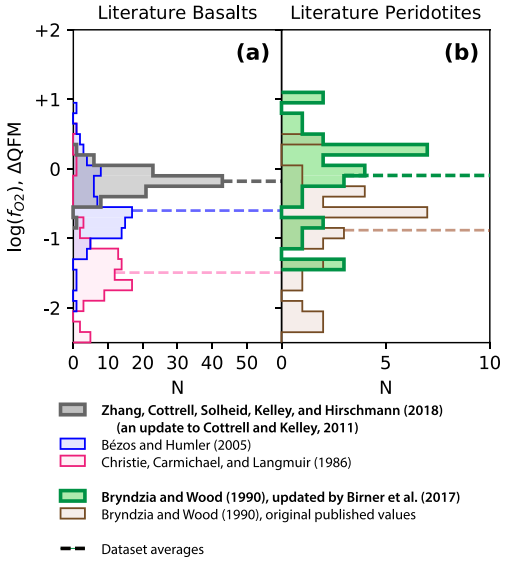

Fig. 1. Literature oxygen fugacity data, showing the evolution of f_{O2} averages for both lithologies. Histograms with thick borders represent the most up-to-date estimates for f_{O2}, while darker shades show where histograms overlap. **(a)** Global mid-ocean ridge basalt oxygen fugacity, from Zhang et al. (2018—an update of the Cottrell and Kelley, 2011, dataset), compared to the earlier works of Christie et al. (1986) and Bézos and Humler (2005). **(b)** Global mid-ocean ridge peridotite oxygen fugacity, revised by Birner et al. (2017) from the dataset of Bryndzia and Wood (1990), compared to the original published values of Bryndzia and Wood (1990). The revised values were calculated using the method of Davis et al. (2017) and additionally use a lower pressure and temperature of equilibration, as described in Appendix B.

fugacity recorded by mid-ocean ridge basalts (MORB) and the oxygen fugacity recorded by ridge peridotites. These two lithologies are petrogenetically related, as MORBs are produced via partial melting of peridotites at depth (e.g., Kushiro, 1968; Stolper, 1980; Kinzler and Grove, 1992). As a result, peridotites and basalts both provide a window into the oxygen fugacity of the Earth's upper mantle. Despite the applicability of these lithologies to the study of f_{O2}, many aspects of oceanic upper mantle f_{O2} remain poorly constrained. In particular, little is known about the magnitude and length scales of heterogeneity in f_{O2} beneath ridges (e.g., Cottrell and Kelley, 2013), and little work has been done to compare current estimates for the oxygen fugacity of the upper mantle as implied by the different proxies.

The oxygen fugacity of mid-ocean ridge basalts has received significant attention. The seminal work of Christie et al. (1986) used wet chemistry to determine $Fe^{3+}/\Sigma Fe$ ratios in basaltic glass, and concluded that MORBs record f_{O2} values between 1 and 2 log units more reduced than the quartz–fayalite–magnetite (QFM) buffer ($Fe^{3+}/\Sigma Fe = 0.07 \pm 0.01$, QFM -1.20 ± 0.44, $n = 87$, Fig. 1a). This estimate was revised upward to $Fe^{3+}/\Sigma Fe = 0.12 \pm 0.02$ ($n = 104$) by Bézos and Humler (2005), based on determinations of $Fe^{3+}/\Sigma Fe$ using a different wet-chemical method. Their revised estimate put the f_{O2} recorded by MORB at QFM -0.41 ± 0.43, about 0.8 log units more oxidized than the Christie et al. (1986) estimate [Fig. 1a]. This estimate was revised upwards again by Cottrell and Kelley (2011), who used micro X-ray Absorption Near Edge Structure (μ-XANES) spectroscopy to measure the $Fe^{3+}/\Sigma Fe$ ratio in MORB glasses. The μ-XANES technique has the advantage of ensuring that only glass is analyzed, as opposed to bulk techniques such as wet chemistry that may incorporate olivine phenocrysts and thus overestimate the ferrous iron present in the basalt. Cottrell and Kelley (2011) used room temperature Mössbauer spectroscopy to calibrate the standards used for XANES, but a recent recalibration accounts for the effects of recoilless fraction (Zhang et al., 2018). The Cottrell and Kelley (2011) result has thus been revised, putting the f_{O2} of MORB at QFM -0.18 ± 0.16 ($Fe^{3+}/\Sigma Fe = 0.143 \pm 0.008$, $n = 103$; Fig. 1a).

All four studies (Christie et al., 1986; Bézos and Humler, 2005; Cottrell and Kelley, 2011; Zhang et al., 2018) agree that MORB records relatively homogeneous oxygen fugacity globally ($1\sigma < 0.5$ log units). Each study analyzed over 75 basalts, together representing over 200 distinct locations from the ridges in Earth's three major ocean basins [Fig. 2a]. While studies such as Cottrell and Kelley (2013) have found evidence of systematic variation in redox between ridges, these changes are small compared to changes in basalt redox seen within and amongst subduction zones and back arc basins (Carmichael, 1991; Kelley and Cottrell, 2009; Brounce et al., 2014).

In contrast to the f_{O2} of MORB, the oxygen fugacity recorded by ridge peridotites has received less attention. Seminal work by Bryndzia and Wood (1990) used spinel oxybarometry, based on phase equilibrium between olivine, orthopyroxene, and spinel, to calculate the oxygen fugacity of 35 peridotite samples from 12 ridge and transform fault locations. Of these, Bryndzia and Wood excluded the anomalously oxidized St. Paul's Rocks from their discussion of typical ridge f_{O2}, as these peridotites are unusual, subaerially exposed, amphibole-bearing mylonites. They determined an average f_{O2} of QFM -0.88 ± 0.70 [Fig. 1b] from the remaining 33 peridotites, >90% of which are from transform faults [Fig. 2b]. Notably, when compared to the Zhang et al. (2018) estimate for MORB f_{O2}, the Bryndzia and Wood peridotites record 4 times more variability (Fig. 1), despite the much sparser global coverage for peridotite analyses [Fig. 2b]. At the time of publication, Bryndzia and Wood noted the agreement between the f_{O2} recorded by global MORB in the Christie et al. (1986) study, and the f_{O2} recorded by their 11 peridotite locations using spinel oxybarometry. However, as more recent studies have upwardly revised the f_{O2} recorded by basalts, and the number of basalts with f_{O2} constraints has greatly expanded, the need arises to further expand and investigate the peridotite dataset (Frost and McCammon, 2008; Davis and Cottrell, in press).

In theory, basaltic melts and peridotite residues, in equilibrium, should record the same f_{O2}. Although different proxies must be employed to calculate f_{O2} for each lithology, experimental work by Davis and Cottrell (in press) has demonstrated the congruence of these two methods. By equilibrating olivine + orthopyroxene + spinel + basaltic melt at 1 atmosphere, Davis and Cottrell (in press) showed that both XANES (Cottrell et al., 2009) and spinel oxybarometry (Davis et al., 2017) return f_{O2} values consistent with the known f_{O2} of the furnace. We can therefore eliminate the possibility of a systematic offset between these two f_{O2} proxies in a melt + peridotite system at equilibrium. However, several complicating factors arise when assessing f_{O2} congruence between natural basalts and peridotites. Using the Bryndzia and Wood (1990) dataset in conjunction with the global MORB f_{O2} dataset to assess the degree of agreement between these two f_{O2} proxies is problematic because there is essentially no overlap between the peridotite and basalt locations [Fig. 2]. While basalts can be sampled at almost all ridge segments worldwide, peridotites are exposed primarily at slow and ultraslow ridges, where crustal production is limited due to the thick conductive cooling lid (e.g., Cannat, 1996; Dick et al., 2003; Montési et al., 2011). As a result, the global MORB f_{O2} dataset extends across all three major ocean basins [Fig. 2a], whereas the peridotite dataset of Bryndzia and Wood (1990) is confined primarily to the Indian Ocean basin [Fig. 2b]. Thus the basalt average may not reflect the peridotite average due to this sampling bias. In addition, the limited number of peridotite samples from each location makes the length scale of mantle heterogeneity unclear. Finally, the seminal work of Bryndzia and Wood (1990) does not consider how the f_{O2} recorded by peri-

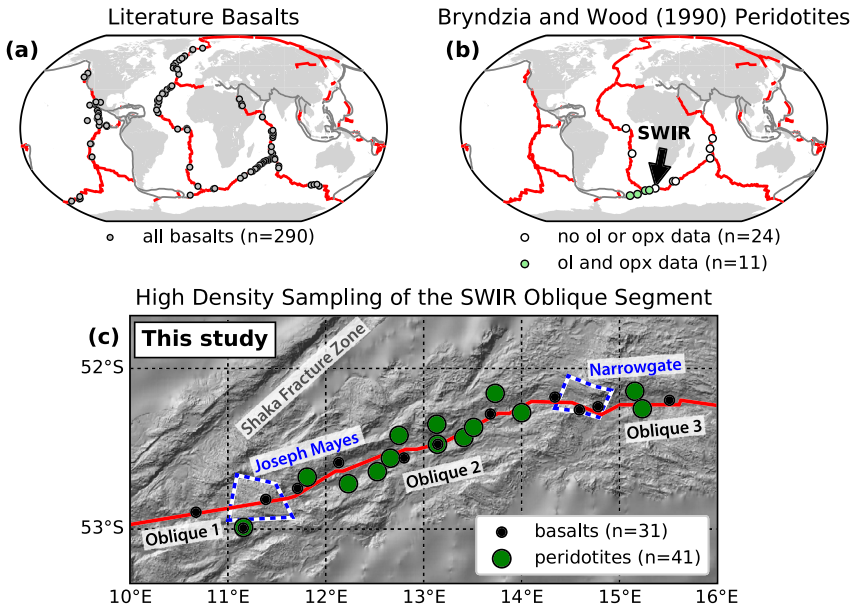

Fig. 2. Global sample locations for mid-ocean ridge basalts and peridotites from the literature. Red lines denote ridge locations, while thinner grey line denote other plate boundaries. Sample numbers for each panel represent the total number of samples analyzed. **(a)** Global coverage for mid-ocean ridge basalts with oxygen fugacity data. Locations are from Christie et al. (1986), Bézos and Humler (2005), Cottrell and Kelley (2011), and Zhang et al. (2018). **(b)** Global coverage for mid-ocean ridge peridotites with oxygen fugacity data. Locations are from Bryndzia and Wood (1990). The global peridotite dataset spans a significantly smaller portion of the mid-ocean ridge system than basalts do. This coverage decreases further when only samples with reported olivine and orthopyroxene compositional data are considered. **(c)** Bathymetric map of the Oblique Segment of the Southwest Indian Ridge, showing locations of basalt and peridotite dredges analyzed in this study. Dredges were chosen in this study to maximize spatial proximity between the two lithologies. Following the terminology of Montési et al. (2011), we subdivide these sections into Oblique 1, Oblique 2, and Oblique 3 from west to east. The base map was created using GeoMapApp (www.geomapapp.org; Ryan et al., 2009). (For interpretation of the colors in the figure(s), the reader is referred to the web version of this article.)

dotites may have evolved due to subsolidus diffusion and cooling (e.g., Woodland et al., 1996) following basalt extraction.

In order to investigate the oxygen fugacity of the upper mantle as implied by ridge peridotites and basalts, we present the f_{O2} of 31 basalt glasses and 41 peridotites from the Oblique Segment of the Southwest Indian Ridge. We explore a range of factors that could modify recorded f_{O2}, in order to project each lithology back to our best estimate of the P–T–X–f_{O2} conditions of last equilibrium between peridotite and basalt. This allows us to assess agreement between the two proxies at maximally consistent conditions. We also explore the degree to which each lithology faithfully records the redox conditions in the upper mantle at the time of melt extraction. This provides insight into the processes by which the f_{O2} recorded by basalts and residues may be modified during melting, melt extraction, cooling, and exhumation.

2. Setting and samples

2.1. Setting

The Southwest Indian Ridge (SWIR) runs for 7700 km between the Bouvet and Rodrigues triple junctions, separating the African and Antarctic plates (e.g., Sclater et al., 1981; Cannat et al., 2008), and is one of the slowest spreading ridges on the planet (e.g., Dick et al., 2003). This study focuses on the Oblique Segment [Fig. 2c], a ~320 km long segment of the SWIR, which runs from the Shaka transform fault at 9°56′E to 15°45′E, where the ridge bends into the Orthogonal Segment. Along this segment, spreading occurs at an oblique angle to the ridge axis, with full spreading rate averaging 14.1 ± 0.1 mm/yr, and effective spreading rate averaging 9.1 ± 2.1 mm/yr once the obliquity of spreading is accounted for (Standish et al., 2008). Two centers of enhanced volcanic activity [Fig. 2c] occur at Joseph Mayes Seamount (11°E–11°36′E) and Narrowgate (14°15′E–14°54′E). The remainder of the Oblique Segment has relatively low rates of basaltic crust production, due to the low effective spreading rate, which results in a thick conductive cooling lid (e.g., Dick et al., 2003; Montési et al., 2011). The relative lack of volcanism results in exposure of residual peridotite at the ridge axis.

2.2. Samples

Peridotite and basalt samples analyzed in this study were sourced from dredges carried out during three cruises: the 2001 KN162 cruise (Standish et al., 2008), the 2003 VAN7 cruise (Standish et al., 2008), and the 1986 PS86 cruise (also referred to as ANTIV/4 in the literature: le Roex et al., 1992). Two dredges (KN162-9 D30 and KN162-9 D53) contain both analyzable peridotite and basalt. The remainder of the dredges do not contain both lithologies or one of the lithologies is too altered or too small for analysis. However, no basalt is expected to be cogenetic with any specific peridotite at the individual dredge level, as melt travels to the surface faster than its solid residue (e.g., Spiegelman and McKenzie, 1987), resulting in a temporal delay of ~1–10 million years between basalt eruption and the exposure of its associated peridotite residue (e.g., Warren et al., 2009). Without constraints on the temporal evolution of sub-ridge Indian mantle f_{O2}, we assume no change in source f_{O2} during this timeframe and treat our basalt and peridotite samples as approximately cogenetic at the segment scale. We thus chose additional samples from twelve peridotite-only and ten basalt-only dredges spanning the length of the Oblique Segment [Fig. 2c].

2.2.1. Basalts

The basalts analyzed in this study consist of 31 glassy samples from the Volcanic Glass Collection (Melson et al., 2002), a subcollection of the National Rock Collection. The samples were received from the Division of Petrology and Volcanology, Department of Mineral Sciences, Smithsonian Institution. All 31 samples have major element data reported in the Volcanic Glass Reference File

(Melson et al., 2002) and additionally published in le Roex et al. (1992) and Standish et al. (2008) [Supplemental Table 1]. Four samples are from Joseph Mayes Seamount, eight samples are from Narrowgate, and nineteen samples are from the remaining portions of the Oblique Segment [Fig. 2c].

2.2.2. Peridotites

The 41 peridotites analyzed in this study consist of dredged samples from the Woods Hole Oceanographic Institution Seafloor Samples Laboratory (doi: 10.7289/V5WH2N0Z). Peridotites from the Oblique Segment comprise lherzolites (>5% clinopyroxene; ~30% of peridotite dredged), harzburgites (<5% clinopyroxene; ~60% of peridotite dredged), and dunites (>90% olivine; ~10% of peridotite dredged), as well as samples with variable degrees of gabbro and pyroxenite veining. The samples are variably altered by seafloor serpentinization, ranging from an alteration score of 3 to a score of 5 (based on the scale of Birner et al., 2016). Dunites lacking orthopyroxene cannot be used to constrain f_{O2} unless silica activity can be determined via another constraint. For this reason, we excluded dunites from our sample selection. We additionally excluded samples with visible veining in hand sample, though retained ~10 samples that contain plagioclase as a trace component. Finally, we excluded samples without primary mantle olivine and orthopyroxene due to pervasive serpentinization (alteration score of 5). The final set of 41 peridotites analyzed consists of lherzolites and harzburgites with alteration scores ranging from 3 to 4.5. Samples are primarily from the Oblique 2 and 3 sections, as almost no peridotites have been dredged from the other sections, where the crust is thicker (Montési et al., 2011).

3. Determination of oxygen fugacity

3.1. Determination of ferric iron in basalts

In order to obtain accurate and precise values for the $Fe^{3+}/\Sigma Fe$ ratios in the basalt glasses, we analyzed all samples by micro X-ray Absorption Near Edge Structure (μ-XANES) spectroscopy at station X26a of the National Synchrotron Light Source (NSLS), Brookhaven National Laboratory, USA, or at station 13-ID-E of the Advanced Photon Source (APS), Argonne National Laboratory, USA. We applied the methodology of Cottrell et al. (2009), modified at APS to mitigate oxidative beam damage caused by the nominally higher photon flux density (Cottrell et al., 2018). To account for recoilless fraction, we applied the calibration of Zhang et al. (2018) to the Mössbauer-referenced calibration glass suite (NMNH Catalog #117393) of Cottrell et al. (2009). Further details on the μ-XANES techniques can be found in Appendix A.

3.2. Calculation of magmatic f_{O2} recorded by basalts

We calculated the magmatic oxygen fugacity of the basalt glasses from their major element compositions and $Fe^{3+}/\Sigma Fe$ ratios using the formulation of Kress and Carmichael (1991). We calculated magmatic f_{O2} relative to the quartz–fayalite–magnetite buffer (ΔQFM; Frost, 1991) using a standard temperature and pressure of 1200 °C and 1 bar.

3.3. Determination of major elements in peridotite phases

We obtained major element compositions for olivine, orthopyroxene, and spinel in each sample via electron microprobe analysis on the Smithsonian Institution's JEOL 8900 electron probe microanalyzer (EPMA), with analytical conditions summarized in Supplemental Table 2. For olivine, we analyzed 6 points per sample, while for orthopyroxene we analyzed 9 points along a transect perpendicular to exsolution, with a defocused beam, in order to determine the average pyroxene composition prior to the formation of exsolution during cooling. Data with totals less than 98.5 or greater than 101.5 were discarded, and compositions for each mineral were then averaged. For spinel, we measured 3 grains per sample and within each grain we measured three points, for a total of 9 EPMA analyses per sample.

3.4. Determination of ferric iron in peridotite spinels

In order to obtain accurate and precise estimates for the ferric iron content in spinel via electron microprobe, we used the Cr#-based correction method of Davis et al. (2017), based on the method of Wood and Virgo (1989). We first calculated the $Fe^{3+}/\Sigma Fe$ ratio according to stoichiometric constraints and then corrected this ratio using a set of 6 calibration spinel standards, provided by B. Wood, with $Fe^{3+}/\Sigma Fe$ ratios previously characterized by Mössbauer spectroscopy (Wood and Virgo, 1989). These calibration spinel standards were run at the beginning and end of each electron microprobe session. After applying this correction, oxides returning negative concentration were corrected to zero, and analyses with oxide totals less than 98.0 or greater than 101.5 were discarded.

3.5. Determination of pressure and temperature recorded by peridotites

To determine the temperature recorded by the peridotite assemblage, we used the olivine-spinel thermometer of Li et al. (1995), as olivine-spinel thermometry is based on the same minerals and elements that are used to calculate f_{O2}. In general, this thermometer records relatively low temperatures (940 ± 100 °C for global ridge peridotites), which likely correspond to shallow pressure conditions. While f_{O2} also depends on mineral systems with higher temperature closure conditions (such as the Cr and Al content in spinel), these effects are minor compared to the effect of Fe^{2+}–Mg^{2+} diffusion between olivine and spinel. Although true equilibrium exists only above the closure conditions for all chemical subsystems within the rock, this equilibrium is not recoverable, and we must choose a thermometer that is maximally congruent with the spinel oxybarometer being used to calculate recorded f_{O2}. We selected the temperature recorded by olivine-spinel Fe^{2+}–Mg^{2+} exchange because this combination of minerals and elements have greater leverage over the f_{O2} calculation than do phases/elements used in other potential thermometers, for example, two-pyroxene thermometry.

We used the spinel–olivine temperatures recorded by the Oblique Segment peridotites and the thermal model of Montési and Behn (2007) to estimate pressure of last equilibrium for our samples. This model presents an analytic solution for the thermal structure associated with corner flow at a ridge axis, along with a scaling relation (ratio of thermal conductivity to spreading velocity) that allows this universal thermal structure to be converted to a location-specific geotherm. Using this model, with an effective full spreading rate of 9.1 mm/yr (Standish et al., 2008), a regional potential temperature of 1370 °C (Dalton et al., 2014), and an adiabatic thermal gradient of 0.3 °C/km, we estimate a pressure of 0.6 GPa for closure of the peridotites to Fe^{2+}–Mg^{2+} exchange. Because pressure has a relatively small effect on calculated f_{O2}, uncertainty in the geotherm deriving from uncertainty in potential temperature does not lead to significant uncertainty in our calculated f_{O2} values [Supplemental Fig. 1]. This pressure is significantly lower than the pressure of 1.0 GPa assumed by Bryndzia and Wood (1990), who based their estimate on the pressure of the spinel stability field and the approximate depth at which peridotite was last in equilibrium with MORB (e.g., Stolper, 1980). While 1 GPa has traditionally been considered the lower limit for spinel stability, experiments by Borghini et al. (2010) have shown that

the chromium-bearing spinel stability field extends to the lowest pressures investigated in their experiments (~0.25 GPa), with plagioclase coexisting with spinel at pressures below ~0.6 GPa. Thus, we find it reasonable for our spinel peridotites to exist in equilibrium at 0.6 GPa. We apply this pressure to all peridotite samples in order to maximize consistency with the spinel–olivine temperatures. Further details on the Davis et al. (2017) technique, estimation of P-T conditions, and error analysis can be found in Appendix B.

3.6. Calculation of f_{O2} recorded by peridotites emplaced at the ridge axis

We calculated the f_{O2} of peridotites using the spinel oxygen barometer of Wood and Virgo (1989) following the updated methodology presented in Davis et al. (2017). Spinel oxybarometry depends on major element compositions of olivine, orthopyroxene, and spinel, as well as temperature and pressure, according to the phase equilibrium:

$$\underset{\text{olivine}}{6Fe_2SiO_4} + O_2 \Leftrightarrow \underset{\text{spinel}}{2Fe_3O_4} + \underset{\text{opx}}{3Fe_2Si_2O_6} \quad (1)$$

We used the method and equations of Davis et al. (2017), which are modified from Mattioli and Wood (1988) and Wood and Virgo (1989), in order to calculate oxygen fugacity for each sample. To determine the activity of magnetite in spinel, we used the MELTS Supplemental Calculator of Sack and Ghiorso (1991a, 1991b) as described in Davis et al. (2017). Oxygen fugacity is reported relative to the QFM buffer of Frost (1991).

When either olivine or orthopyroxene in a sample has been completely replaced by alteration minerals, we used the correlation ($R^2 = 0.93$) between olivine Fo# and iron site occupancy in orthopyroxene ($X^{M1}*X^{M2}$) to estimate the activity of iron in the altered mineral from the composition of the other mineral. This technique is only applicable when both olivine and orthopyroxene were present at mantle conditions, with subsequent replacement of only one mineral by low-temperature alteration. For dunite or pyroxenite lithologies that lack either orthopyroxene or olivine, the oxybarometer is not applicable and this technique may not be applied, as the phase assemblage we use to calculate oxygen fugacity [Equation (1)] is not present.

3.7. Recalculation of literature peridotite f_{O2} data

In order to maintain consistency with our current methodology for calculating oxygen fugacity, we recalculated the mid-ocean ridge peridotite f_{O2} dataset of Bryndzia and Wood (1990) using the same method as applied to the SWIR peridotites in this study. Detailed discussion of this correction is found in Appendix B. Our calculation puts the Bryndzia and Wood (1990) mid-ocean ridge peridotite average at QFM -0.08 ± 0.68 ($n = 31$; data from St. Paul's Rocks and Mid-Cayman Rise are excluded due to their unusual tectonic settings; see Appendix B for further details), compared to their original estimate of QFM -0.88 ± 0.70 [Supplemental Table 3].

Of this 0.8 log unit difference, ~0.3 log units are due to the change in the oxybarometer formulation (Davis et al., 2017). This is consistent with the findings of Davis et al. (2017), who show that the absolute f_{O2} of experimental samples originally analyzed by Wood (1990) are better matched by 0.31 log units using the Davis et al. (2017) formulation than the original Wood and Virgo (1989) formulation. The remaining ~0.5 log units of offset between the Bryndzia and Wood (1990) results and the recalculated results reported here are derived from the lower pressure and temperature of equilibration that we assume for these samples. The original Bryndzia and Wood (1990) data, as well as recalculated data using the Davis et al. (2017) method at both sets of pressure and temperature assumptions, are plotted in Supplemental Fig. 2.

4. Results

4.1. Basalts

For the 30 basalt glasses analyzed, $Fe^{3+}/\Sigma Fe$ ratios as determined by μ-XANES average 0.149 ± 0.014 [Table 1]. This average is the same, within error, as the global MORB average of 0.143 ± 0.008, based on the Mössbauer-based calibration of Cottrell et al. (2009) updated for recoilless fraction (Zhang et al., 2018). Similarly, the magmatic f_{O2} of the basalt glasses, calculated at 1200 °C and 1 atm, averages -0.19 ± 0.19 relative to the QFM buffer [Table 1], which is nearly identical to the Zhang et al. (2018) global MORB average of QFM -0.18 ± 0.16 [Fig. 3]. Magmatic f_{O2} is not correlated with distance along the ridge axis, although glasses from Narrowgate record more variable magmatic f_{O2} values [Fig. 3]. Full spectral data for each point are tabulated in Supplemental Table 4, and calculations of $Fe^{3+}/\Sigma Fe$ ratios from centroid data are shown for each point in Supplemental Table 5.

4.2. Peridotites

For the 41 SWIR peridotites, major element compositions are within the range of typical ridge peridotites (e.g. Dick, 1989; Warren, 2016). Forsterite content in olivine averages 90.6 ± 0.7, while iron site occupancy ($X^{M1}*X^{M2}$) in orthopyroxene averages 0.0075 ± 0.0012. These parameters are well correlated ($R^2 = 0.93$), suggesting equilibrium between the silicate minerals. Major element data for olivine, orthopyroxene, and spinel are reported in Supplemental Tables 6–8. Data for spinel calibration standards are reported in Supplemental Table 9.

Spinel $Fe^{3+}/\Sigma Fe$ ratios average 0.16 ± 0.04, slightly higher than the global ridge average of 0.13 ± 0.04 (Bryndzia and Wood, 1990). Temperatures based on spinel–olivine thermometry average 899 ± 59 °C, compared to an average of 940 ± 100 °C for global ridge peridotites. Oxygen fugacity values, calculated at these temperatures and a pressure of 0.6 GPa, average QFM $+ 0.62 \pm 0.64$ [Table 2], with no clear along-strike trend nor any correspondence to tectonic and volcanic features [Fig. 4a]. Notably, this average is 0.7 log units higher than the average for the recalculated Bryndzia and Wood (1990) dataset (QFM-0.08 ± 0.68; Fig. 4b, c), and 1.5 log units more oxidized than the average oxygen fugacity reported in their original study (QFM -0.88 ± 0.70). Our dataset includes one sample (PS86 D6-37) that was measured in the Bryndzia and Wood (1990) study, which returns consistent f_{O2} values between their study (QFM + 0.42, recalculated as described in Appendix B) and our study (QFM + 0.30).

5. Discussion

Our results indicate that, while the magmatic f_{O2} values of SWIR basalts are consistent with global data for MORB [Fig. 3], SWIR peridotites emplaced at the ridge axis record f_{O2} values more oxidized than the global ridge peridotite array [Fig. 4]. This leads to an apparent offset between MORB and ridge peridotite f_{O2} recorded at SWIR. This offset is not an artifact of using two different techniques for obtaining oxygen fugacity data for the two lithologies, as experimental work by Davis and Cottrell (in press) has shown that μ-XANES and spinel oxybarometry return consistent results within the error of each technique. Crucially, however, reporting f_{O2} values relative to the QFM buffer is misleading when comparing lithologies at different pressures and temperatures, as

Table 1
Oxygen fugacity results for SWIR basalts. The reader is referred to Supplemental Table 5 and Appendix A for more detailed information, including calculation of $Fe^{3+}/\Sigma Fe$ from centroid values, results for individual μ-XANES analyses, and conditions for each beam line session.

Orig. Ship code	USNM catalog #	Location	Lat.	Long.	Centroid	1σ	$Fe^{3+}/\Sigma Fe$	1σ	Magmatic[a] $\log(f_{O2})$, abs.	Magmatic[a] $\log(f_{O2})$, ΔQFM	Source[b] $\log(f_{O2})$, abs.	Source[b] $\log(f_{O2})$, ΔQFM
KN162 D28-24	117373-184	Oblique1	−52.90	10.67	7112.303	0.016	0.149	0.006	−8.50	−0.20	−6.83	−0.12
KN162 D28-26	117373-185	Oblique1	−52.90	10.67	7112.321	0.009	0.156	0.004	−8.34	−0.04	−6.77	0.02
KN162 D28-32	117373-186	Oblique1	−52.90	10.67	7112.321	0.010	0.156	0.004	−8.30	0.00	−6.20	−0.02
KN162 D30-12	117373-198	Joseph Mayes	−52.99	11.16	7112.311	0.006	0.152	0.002	−8.36	−0.05	−5.46	0.08
KN162 D30-16	117373-199	Joseph Mayes	−52.99	11.16	7112.273	0.016	0.138	0.006	−8.49	−0.18	−5.54	−0.10
KN162 D30-18	117373-200	Joseph Mayes	−52.99	11.16	7112.286	0.011	0.143	0.004	−8.53	−0.23	−5.63	−0.10
KN162 D33-55	117373-213	Joseph Mayes	−52.82	11.39	7112.326	0.018	0.158	0.007	−8.25	0.05	−5.46	−0.10
KN162 D36-01	117373-233	Oblique2	−52.75	11.71	7112.286	0.011	0.143	0.004	−8.56	−0.26	−6.76	−0.21
KN162 D36-11	117373-236	Oblique2	−52.75	11.71	7112.302	0.020	0.149	0.007	−8.45	−0.15	−6.45	−0.10
KN162 D41-05	117373-250	Oblique2	−52.59	12.13	7112.261	0.012	0.134	0.004	−8.71	−0.41	−6.87	−0.27
KN162 D41-07	117373-251	Oblique2	−52.59	12.13	7112.299	0.007	0.148	0.003	−8.51	−0.20	−6.30	−0.27
KN162 D41-12	117373-252	Oblique2	−52.59	12.13	7112.304	0.008	0.150	0.003	−8.48	−0.18	−6.40	−0.19
KN162 D41-13	117373-253	Oblique2	−52.59	12.13	7112.326	0.003	0.158	0.001	−8.34	−0.03	−6.54	0.00
KN162 D48-04	117373-254	Oblique2	−52.56	12.80	7112.265	0.006	0.135	0.002	−8.67	−0.37	−6.59	−0.24
KN162 D48-08	117373-255	Oblique2	−52.56	12.80	7112.291	0.007	0.145	0.003	−8.45	−0.15	−5.70	−0.10
KN162 D48-21	117373-258	Oblique2	−52.56	12.80	7112.208	0.019	0.115	0.007	−8.99	−0.69	−6.78	−0.46
KN162 D48-23	117373-259	Oblique2	−52.56	12.80	7112.272	0.007	0.138	0.003	−8.57	−0.27	−5.93	−0.24
KN162 D53-01	117373-272	Oblique2	−52.48	13.14	7112.295	0.009	0.146	0.003	−8.54	−0.23	−7.10	−0.19
KN162 D53-02	117373-273	Oblique2	−52.48	13.14	7112.298	0.006	0.147	0.002	−8.54	−0.23	−6.77	−0.22
KN162 D53-03	117373-274	Oblique2	−52.48	13.14	7112.291	0.014	0.145	0.005	−8.57	−0.27	−7.03	−0.25
KN162 D53-05	117373-275	Oblique2	−52.48	13.14	7112.274	0.014	0.139	0.005	−8.68	−0.38	−6.86	−0.40
PS86 D5-01	117377-30	Oblique2	−52.29	13.68	7112.305	0.012	0.150	0.005	−8.44	−0.13	−6.90	−0.08
VAN7 D90-35	117379-64	Narrowgate	−52.18	14.34	7112.368	0.001	0.174	0.000	−8.21	0.09	–	–
VAN7 D90-52	117379-65	Narrowgate	−52.18	14.34	7112.400	0.003	0.187	0.001	−8.10	0.20	–	–
VAN7 D90-77	117379-66	Narrowgate	−52.18	14.34	7112.270	0.007	0.137	0.003	−8.81	−0.50	–	–
VAN7 D89-02	117379-58	Narrowgate	−52.26	14.59	7112.358	0.009	0.170	0.003	−8.27	0.03	–	–
VAN7 D89-13	117379-61	Narrowgate	−52.26	14.59	7112.276	0.008	0.139	0.003	−8.69	−0.38	–	–
VAN7 D87-01	117379-50	Narrowgate	−52.24	14.78	7112.337	0.007	0.162	0.003	−8.34	−0.04	–	–
VAN7 D87-02	117379-51	Narrowgate	−52.24	14.78	7112.287	0.014	0.143	0.005	−8.68	−0.37	–	–
VAN7 D87-03	117379-52	Narrowgate	−52.24	14.78	7112.315	0.001	0.160	0.010	−8.40	−0.10	–	–
VAN7 D69-79	117379-17	Oblique 3	−52.20	15.51	7112.265	0.006	0.150	0.002	−8.35	−0.05	−5.91	−0.05

[a] Magmatic f_{O2} is calculated at 1200 °C and 1 bar (0.0001 GPa) for all samples.
[b] Source f_{O2} is calculated at ~1320 °C and ~1.25 GPa, with temperature and pressure determined for each sample based on the thermobarometer of Lee et al. (2009).

Table 2
Oxygen fugacity results and calculated mineral parameters for SWIR peridotites.

Sample	Type	Lat.	Long.	spl		olv	opx	Closure conditions						Source conditions	
				$Fe^{3+}/\Sigma Fe$	a_{Fe3O4}	Fo#	$X^{M1}*X^{M2}$	T (°C)	log(f_{O2}), abs.	log(f_{O2}), ΔQFM	1σ	error (+)	error (−)	log(f_{O2}), abs.	log(f_{O2}), ΔQFM
KN162-9 D30-72	Joseph Mayes	−52.99	11.16	0.16	0.017	*91.19*	0.0063	811	−12.81	0.93	0.11	0.42	0.43	–	–
KN162-9 D30-75	Joseph Mayes	−52.99	11.16	0.17	0.016	91.36	0.0065	813	−12.66	1.03	0.17	0.41	0.42	−5.69	0.46
KN162-9 D37-01	Oblique 2	−52.68	11.81	0.06	0.001	92.35	0.0048	940	−12.59	−1.24	0.40	0.82	1.03	−7.75	−1.60
KN162-9 D37-02	Oblique 2	−52.68	11.81	0.08	0.002	92.74	0.0043	898	−12.58	−0.51	0.14	0.65	0.73	−7.11	−0.95
KN162-9 D37-10	Oblique 2	−52.68	11.81	0.19	0.018	90.41	0.0084	934	−10.34	1.09	0.17	0.46	0.48	−5.30	0.86
KN162-9 D37-13	Oblique 2	−52.68	11.81	0.12	0.006	91.25	0.0062	888	−12.11	0.12	0.26	0.55	0.60	−6.57	−0.42
KN162-9 D37-14	Oblique 2	−52.68	11.81	0.15	0.008	91.61	0.0058	927	−11.02	0.52	0.09	0.56	0.60	−6.21	−0.06
KN162-9 D42-04	Oblique 2	−52.72	12.23	0.14	0.007	*91.16*	0.0066	918	−11.39	0.33	0.14	0.48	0.50	–	–
KN162-9 D42-08	Oblique 2	−52.72	12.23	0.16	0.012	90.36	0.0075	951	−10.57	0.58	0.07	0.53	0.56	−6.04	0.11
KN162-9 D42-10	Oblique 2	−52.72	12.23	0.19	0.027	90.48	0.0080	839	−11.87	1.29	0.06	0.41	0.42	−5.40	0.76
KN162-9 D42-14	Oblique 2	−52.72	12.23	0.22	0.021	90.42	0.0078	976	−9.59	1.16	0.19	0.44	0.46	−5.38	0.78
KN162-9 D43-85	Oblique 2	−52.65	12.53	0.24	0.030	90.64	0.0075	869	−11.16	1.44	0.07	0.36	0.36	−5.24	0.92
KN162-9 D47-26	Oblique 2	−52.56	12.66	0.13	0.008	*90.01*	0.0078	948	−11.07	0.12	0.27	0.62	0.70	–	–
KN162-9 D47-29	Oblique 2	−52.56	12.66	0.10	0.006	90.92	0.0063	868	−12.60	−0.01	0.15	0.70	0.80	−7.26	−1.10
KN162-9 D47-33	Oblique 2	−52.56	12.66	0.14	0.014	*91.06*	0.0064	847	−12.28	0.73	0.21	0.54	0.58	–	–
KN162-9 D47-36	Oblique 2	−52.56	12.66	0.15	0.033	89.56	0.0088	797	−12.92	1.09	0.26	0.51	0.53	−6.32	−0.16
KN162-9 D47-49	Oblique 2	−52.56	12.66	0.16	0.024	90.43	0.0076	769	−13.63	1.01	0.10	0.40	0.41	−6.01	0.15
KN162-9 D50-07	Oblique 2	−52.42	12.75	0.14	0.010	90.72	0.0069	914	−11.27	0.49	0.15	0.56	0.60	−6.18	−0.03
KN162-9 D50-11	Oblique 2	−52.42	12.75	0.19	0.030	*89.76*	0.0086	890	−11.02	1.17	0.22	0.48	0.49	–	–
KN162-9 D50-35	Oblique 2	−52.42	12.75	0.12	0.008	*90.07*	0.0082	941	−11.18	0.13	0.16	0.62	0.69	–	–
PS86 D6-26	Oblique 2	−52.35	13.13	0.16	0.016	90.47	0.0068	908	−11.10	0.77	0.25	0.55	0.59	−6.46	−0.31
PS86 D6-37	Oblique 2	−52.35	13.13	0.16	0.008	90.13	0.0079	1033	−9.60	0.30	0.10	0.56	0.60	−6.60	−0.45
PS86 D6-39	Oblique 2	−52.35	13.13	0.18	0.012	90.61	0.0070	971	−10.20	0.63	0.06	0.51	0.53	−6.34	−0.19
KN162-9 D53-21	Oblique 2	−52.47	13.14	0.17	0.031	89.39	*0.0092*	861	−11.62	1.10	0.18	0.51	0.54	–	–
KN162-9 D53-24	Oblique 2	−52.47	13.14	0.17	0.032	89.73	0.0096	850	−11.60	1.32	0.21	0.51	0.54	−5.06	1.09
KN162-9 D53-39	Oblique 2	−52.47	13.14	0.14	0.017	90.32	0.0078	859	−11.91	0.83	0.13	0.58	0.62	−5.91	0.24
KN162-9 D55-21	Oblique 2	−52.43	13.41	0.20	0.023	89.89	0.0086	879	−11.38	1.03	0.12	0.38	0.38	−5.61	0.54
KN162-9 D55-23	Oblique 2	−52.43	13.41	0.13	0.009	90.37	0.0073	922	−11.42	0.22	0.15	0.58	0.64	−6.49	−0.33
KN162-9 D55-25	Oblique 2	−52.43	13.41	0.15	0.013	91.40	0.0060	867	−11.82	0.79	0.09	0.54	0.57	−6.01	0.15
KN162-9 D55-28	Oblique 2	−52.43	13.41	0.20	0.020	90.11	0.0083	942	−10.27	1.02	0.06	0.46	0.48	−5.50	0.66
KN162-9 D56-33	Oblique 2	−52.37	13.51	0.07	0.002	91.66	0.0056	820	−14.23	−0.68	0.43	0.69	0.80	−7.40	−1.24
KN162-9 D56-54	Oblique 2	−52.37	13.51	0.07	0.001	91.51	0.0060	899	−13.03	−0.98	0.55	0.61	0.69	−7.57	−1.42
KN162-9 D58-16	Oblique 2	−52.16	13.73	0.21	0.030	90.31	0.0078	917	−10.36	1.36	0.24	0.46	0.47	−5.37	0.79
KN162-9 D58-23	Oblique 2	−52.16	13.73	0.23	0.037	*89.92*	0.0091	827	−11.96	1.46	0.29	0.35	0.35	–	–
KN162-9 D58-30	Oblique 2	−52.16	13.73	0.20	0.017	90.55	0.0075	912	−10.87	0.95	0.10	0.41	0.42	−5.61	0.55
KN162-9 D59-02	Oblique 2	−52.28	14.00	0.17	0.012	90.11	0.0077	981	−10.13	0.55	0.11	0.51	0.54	−6.09	0.07
KN162-9 D59-04	Oblique 2	−52.28	14.00	0.14	0.009	90.97	0.0070	895	−11.59	0.52	0.23	0.53	0.56	−6.20	−0.04
KN162-9 D59-07	Oblique 2	−52.28	14.00	0.20	0.025	89.44	0.0091	930	−10.50	1.00	0.24	0.45	0.47	−5.53	0.63
VAN7 D86-28	Oblique 3	−52.14	15.16	0.15	0.014	89.97	0.0083	897	−11.47	0.59	0.11	0.53	0.57	−6.57	−0.41
VAN7 D86-37	Oblique 3	−52.14	15.16	0.16	0.008	*90.81*	0.0069	949	−10.78	0.42	0.11	0.48	0.50	–	–
VAN7 D85-47	Oblique 3	−52.25	15.23	0.15	0.008	90.23	*0.0079*	977	−10.38	0.35	0.15	0.54	0.59	–	–

*italicized Fo# and XM1*XM2 values are estimated from correlations between olivine and orthopyroxene compositions.*

[1] Closure f_{O2} conditions are calculated at the listed T, recorded by spinel–olivine thermometry, and a pressure of 0.6 GPa.

[2] Source f_{O2} conditions are calculated at 1320 °C and 1.25 GPa, estimated from basalt thermobarometry, with subsolidus projection as described in Section 5.1.2.

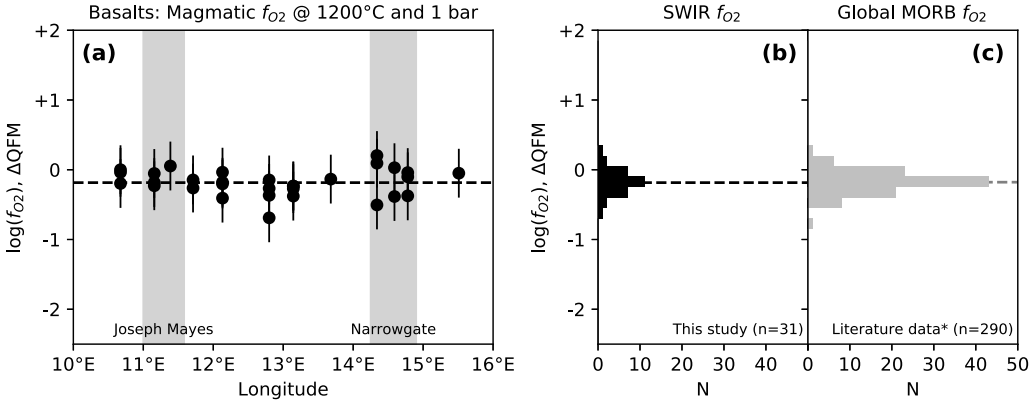

Fig. 3. **(a)** Magmatic oxygen fugacity results for SWIR basalts along the axis of the Oblique Segment. Error bars for each point represent the uncertainty associated with calculation of f_{O2} from pressure, temperature, and composition, calculated using the standard error of the Kress and Carmichael (1991) model [Supplemental Fig. 7]. **(b)** Histogram of magmatic oxygen fugacity for the SWIR Oblique Segment basalts. **(c)** Histogram of magmatic oxygen fugacity for global mid-ocean ridge basalts (Zhang et al., 2018).

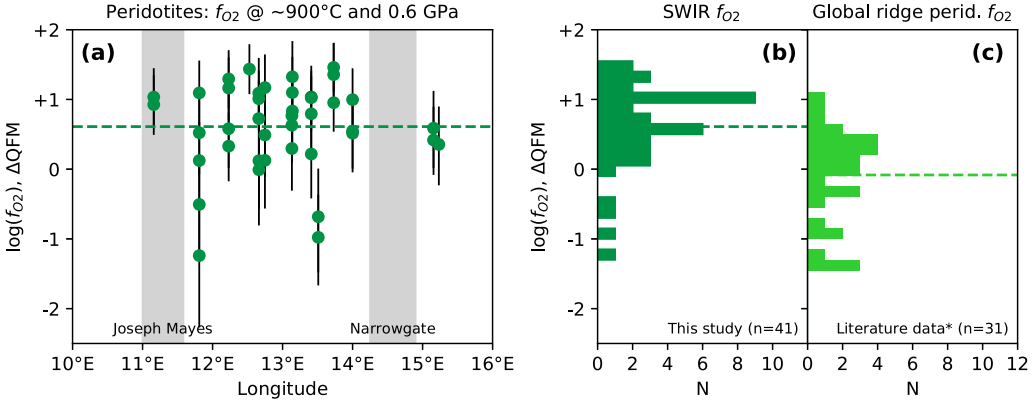

Fig. 4. **(a)** Recorded oxygen fugacity for SWIR peridotites along the axis of the Oblique Segment. Temperatures are from spinel–olivine thermometry (Li et al., 1995) and pressure is estimated from the average temperature of the dataset (~900 °C) and the geotherm of Montési and Behn (2007). Error bars represent the uncertainty associated with the spinel oxybarometry technique for each sample, calculated using component uncertainty analysis, as described in Davis et al. (2017). **(b)** Histogram of recorded oxygen fugacity for SWIR peridotites. **(c)** Histogram of revised oxygen fugacity estimates at closure conditions for global mid-ocean ridge peridotites. The data are from Bryndzia and Wood (1990), recalculated following the Davis et al. (2017) method, as described in Appendix B.

shown schematically in Fig. 5. The QFM buffer is strongly temperature dependent, such that the absolute f_{O2} of the buffer increases by over 5 log units between 900 °C and 1300 °C [Fig. 5]. Thus, peridotites (recording conditions of ~900 °C and ~0.6 GPa) and basalts (recording conditions of ~1200 °C and 1 bar) are only expected to record the same f_{O2} relative to QFM if the lithologies were in equilibrium at depth and followed equivalent f_{O2} paths relative to QFM during ascent and cooling [a schematic illustration of this concept is shown in Fig. 5].

In order to properly compare the oxygen fugacity of basalt to the oxygen fugacity of peridotites, each lithology must be projected back to conditions of equilibrium between basalt and peridotite at the time of melt segregation in the upper mantle. Below, we discuss methods of projection to these source conditions for both peridotites and basalts, and conclude that the oxygen fugacity values of source mantle implied by SWIR peridotites and SWIR basalts are consistent. No offset exists, within the error of each technique, and the oxygen fugacity of the source mantle under SWIR lies, on average, at ~QFM.

5.1. Oxygen fugacity of the mantle source at the pressure and temperature of melt extraction

Basaltic magma is produced in equilibrium with its parental peridotite via partial melting at mid-upper mantle pressures and temperatures (e.g., Kushiro, 1968). After this point, however, peridotite and basalt follow different P–T–t paths to the surface. The basalt ascends quickly due to its buoyancy within the residual mantle, losing little heat to its surroundings before quickly quenching upon eruption at the seafloor [Fig. 5b]. As a result, basalts record relatively high temperatures (~1200 °C), and their quench rate does not impact the $Fe^{3+}/\Sigma Fe$ ratio determined by XANES (Wilke et al., 2002; Cottrell and Kelley, 2011). Additionally, our samples, like the majority of MORB, erupted at >300 bar (Standish et al., 2008), such that degassing of C–O–H–S species cannot generate detectable shifts in f_{O2} (Brounce et al., 2017).

In contrast to basalts, peridotites ascend slowly via upwelling of the upper mantle, before 'freezing' into the lithosphere due to conductive cooling. This slow ascent allows diffusion of elements within and between minerals to continue to relatively shallow conditions, resulting in closure conditions at lower temperatures (~900 °C for Fe^{2+}–Mg^{2+} exchange between spinel and olivine) than recorded by basalts [Fig. 5b]. To assess each lithology as a proxy for the oxygen fugacity of the upper mantle and determine the relative agreement between these two proxies at the time of melt-residue separation, we projected the recorded f_{O2} of each lithology back to the source conditions of last equilibrium between basalt and peridotite.

5.1.1. Basalts

Between production of mid-ocean ridge basalt via partial melting of peridotite at depth and its subsequent eruption and quench-

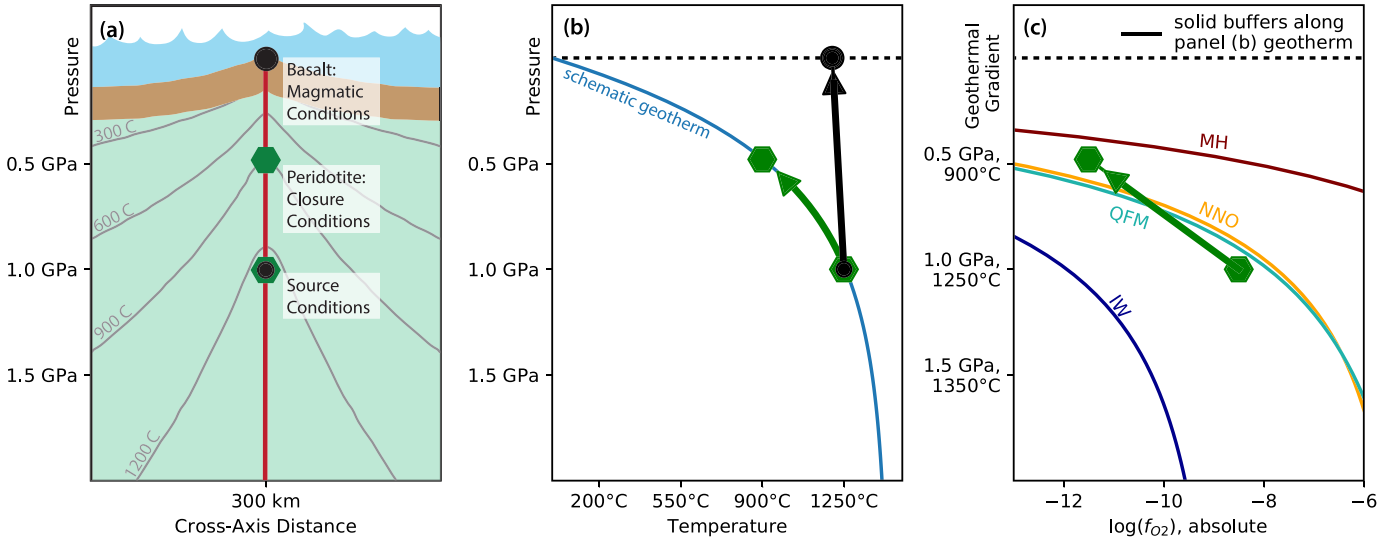

Fig. 5. Schematic illustration of peridotite/basalt P–T–f_{O2} conditions at ridges and the importance of considering absolute f_{O2} as well as f_{O2} relative to a buffer. Numeric values shown are approximate. To demonstrate the movement of a peridotite in each panel during ascent and cooling at a generic ultraslow spreading ridge, we chose pressures of 0.5 GPa and 1.0 GPa to represent recorded conditions and source conditions, respectively. The actual values of 0.6 GPa (recorded) and 1.25 GPa (source) used in the text are based upon geotherm parameters and basalt thermobarometry specific to SWIR. **(a)** Cross-section of a mid-ocean ridge. Isotherms are from Montési and Behn (2007), scaled for a typical ultraslow spreading ridge. "Source conditions" represents the approximate depth/pressure for peridotite and basalt in equilibrium before the two phases separate. "Peridotite closure conditions" represents the approximate last depth/pressure that the peridotite equilibrated at while ascending to the surface. "Basalt magmatic conditions" represents the depth/pressure of seafloor quenching for a mid-ocean ridge basalt. **(b)** Pressure vs. temperature conditions for the axis of the schematic mid-ocean ridge shown in panel (a). From source conditions at ~1250 °C and ~1 GPa, a peridotite will ascend along the geotherm. Once the closure temperature (~900 °C) for the peridotite is reached, its chemical composition will be "frozen" in, and the peridotite will record these conditions when analyzed. A basalt however, will ascend quickly from source conditions, losing little heat to the system. It will then quench at the seafloor, recording conditions of ~1200 °C. **(c)** Log(f_{O2}) along the pressure–temperature gradient described by the geotherm in panel (b). The solid lines represent the position of various solid buffers (MH: magnetite–hematite, NNO: nickel–nickel oxide, QFM: quartz–fayalite–magnetite, IW: iron–wüstite) along the geotherm. The thick green arrow represents a possible path in P–T–log(f_{O2}) space for a peridotite ascending from source to closure conditions along the geotherm. This path represents a decrease in absolute log(f_{O2}), while showing an apparent increase in log(f_{O2}) relative to the QFM buffer, illustrating that offsets between lithologies relative to QFM may be misleading if the lithologies are recording different pressure–temperature conditions. The adiabatic ascent of basalt shown in panel (b) cannot be plotted on this projection, as basalt does not follow the P-T path of the geotherm to the surface. Because basalt is expected to roughly parallel the QFM buffer during ascent (Kress and Carmichael, 1991), the projection from recorded conditions to source conditions has a smaller effect on relative f_{O2} for basalts than for peridotites.

ing at the seafloor, several processes may modify the oxygen fugacity recorded by basaltic glass.

Fractional crystallization of olivine ± plagioclase ± clinopyroxene preferentially removes Fe^{2+} from the liquid relative to Fe^{3+}. As shown for MORB by Cottrell and Kelley (2011), the $Fe^{3+}/\Sigma Fe$ ratio increases by 3% absolute as MgO decreases from 10 to 5 wt.%, resulting in slight oxidation of the remaining liquid. Additionally, the f_{O2} of basalt will change as it decompresses to the surface after separating from its peridotite residue. Kress and Carmichael (1991) showed that a typical basalt will reduce by ~0.5 log units relative to QFM as it ascends from 3 GPa to the surface along an adiabatic gradient.

To estimate the total change in f_{O2} of a given basalt sample after separation from its peridotite residue, the pressure and temperature of separation and the composition of the primary basaltic magma need to be known. For primitive samples (MgO > 8.5 wt%), a primary magma can be reconstructed via olivine addition to a melt composition in equilibrium with Fo90 olivine (the average composition of mantle olivine, where Mg/(Mg + Fe) = 0.90). Unfortunately, very few basalt samples from the Oblique Segment are sufficiently primitive to directly calculate a primary magma via olivine addition. Of the 175 samples from SWIR with major element data reported in the VG dataset (Melson et al., 2002), only three samples have a MgO content greater than 8.5 wt%. Within the set of 30 SWIR basalt glasses that we investigated for this study, one sample (KN162-9 D48-21) is sufficiently primitive to be able to calculate a primary magma.

For typical basalt compositions (MgO < 8.5 wt%), the composition of the primary magma prior to the onset of fractional crystallization cannot be determined solely by olivine addition, as more phases were likely present during differentiation. We thus estimated the primary magma composition via a two-step process. We first performed a fractional crystallization correction along empirically determined, segment-specific liquid lines of descent to 8.5 wt% MgO [Supplemental Figs. 4–5], at which point olivine is assumed to be the only phase on the liquidus. We then added olivine back into the melt composition until equilibrium with Fo90 was reached. The composition of this reconstructed primary magma was then used to calculate f_{O2} at the temperature and pressure of melt segregation. For Narrowgate samples, a lack of primitive basalt glass samples precluded constraint of LLDs at MgO > 7.5 wt% [Supplemental Fig. 6]. As a result, we did not calculate primary magmas for the Narrowgate samples. Further details on this technique are discussed in Appendix C, and primary magma compositions are reported in Supplemental Table 10.

Using our technique for reconstructing primary magma composition, we find that the source f_{O2} implied by the SWIR basalts is QFM −0.16, with a standard deviation of ±0.13 and a standard error of the mean of ±0.03 [Table 3], at temperatures ranging from ~1260–1380 °C and corresponding pressures ranging from ~0.9–1.7 GPa. Relative to QFM, this value is nearly identical to the magmatic f_{O2} average for the SWIR dataset (QFM −0.19, with a standard deviation of ±0.19 and a standard error of the mean of ±0.03), corroborating the observation of Cottrell and Kelley (2011) that the slight reduction of basaltic melt during decompression is, on average, offset by the slight oxidation of basaltic melt during fractional crystallization. Pressures and temperatures are well correlated ($R^2 = 0.96$) and the maximum temperature of 1380 °C is in good agreement with the potential temperature estimate of 1350–1380 °C for the Oblique Segment (Dalton et al., 2014). To determine the best estimate for source pressure and temperature, which we use later to project peridotites to source

Table 3
Summary of oxygen fugacity results for SWIR peridotites and basalts, calculated at both recorded conditions and projected source conditions.

	P	T	$\log(f_{O2})$, abs.	$\log(f_{O2})$, ΔQFM	1σ	Std. err. of the mean*	Error from f_{O2} calc.**	Projection Error***
Basalts: magmatic conditions[a]	1 bar	1200 °C	−8.49	−0.19	0.19	0.03	0.35	–
Peridotites: closure conditions[b]	0.6 GPa	∼900 °C	−11.54	+0.61	0.63	0.10	∼0.5	–
Basalts: source conditions[c]	∼1.25 GPa	∼1320 °C	−6.38	−0.16	0.13	0.03	0.35	0.15
Peridotites: source conditions[d]	1.25 GPa	1320 °C	−6.15	0.00	0.72	0.13	∼0.5	0.5****

[a] Basalt magmatic f_{O2} is calculated at 1200 °C and 1 bar (0.0001 GPa) for all samples.
[b] Peridotite closure f_{O2} conditions are calculated at the temperature recorded by spinel–olivine thermometry for each sample.
[c] Basalt source f_{O2} is calculated at ∼1320 °C and ∼1.25 GPa, with temperature and pressure determined for each sample based on the thermobarometer of Lee et al. (2009).
[d] Peridotite source f_{O2} conditions are calculated at 1320 °C and 1.25 GPa, estimated from basalt thermobarometry, with subsolidus projection as described in Section 5.1.2.
* The standard error of the mean is calculated using the equation: $SE_{\bar{x}} = \sigma/\sqrt{N}$.
** The error from the calculation of f_{O2} represents the error associated with calculating f_{O2} from pressure, temperature, and composition. For basalts, this is the standard error associated with the Kress and Carmichael (1991) model [Supplemental Fig. 7], whereas for peridotites this is the total error associated with the spinel oxybarometer, based on component analysis of errors as described in Davis et al. (2017).
*** The projection error is the error associated with projecting recorded f_{O2} to source conditions.
**** The projection error for peridotite is based upon the difference between the two end-member scenarios for projection of peridotite to source conditions, as described in Section 5.1.2. While the error of projection for basalts is uncorrelated for each point, the error of projection for peridotite would apply equally to each point, such that this projection error is a measure of accuracy associated with the mean of the sample set.

conditions, we took the middle of the temperature range (1320 °C) and used the correlation between pressure and temperature ($P = 0.0061 * T - 6.82$) to choose a corresponding pressure of 1.25 GPa.

To estimate the uncertainty on our projection of basalt f_{O2} to source conditions for each individual sample, we applied a Monte Carlo simulation in order to propagate errors from each step of the data reduction process (see Appendix C for details). This analysis suggests an uncertainty of ∼0.12 log units associated with the projection of f_{O2} for an individual basalt sample back to source conditions. We apply an additional uncertainty of ±0.35 log units to the f_{O2} we calculate for each individual sample associated with the conversion of basalt $Fe^{3+}/\Sigma Fe$ ratio to f_{O2} using the formulation of Kress and Carmichael (1991) [Supplemental Fig. 8]. The total uncertainty in f_{O2}, therefore, for each sample is on the order of 0.47 log units.

We calculate average MORB source f_{O2} conditions for the SWIR Oblique Segment equal to QFM −0.16, with a standard deviation of ±0.13 and a standard error of the mean of ±0.03 log units, at 1320 °C and 1.25 GPa [Table 3].

5.1.2. Peridotites

In a closed system as peridotite ascends and cools, the constituent minerals and elements will redistribute in order to maintain chemical equilibrium between all phases. While the qualitative direction of changes (e.g., whether an element diffuses into versus out of a mineral during cooling) is known for parts of the peridotite assemblage during cooling, the magnitudes of these changes and individual P–T–t paths are not well constrained. Accurately reconstructing peridotite composition and f_{O2} at source pressures and temperatures from data recorded by recovered peridotites carries with it large uncertainties given our present state of knowledge. Strategies considered for reconstruction are described below, and further details can be found in Appendix D.

Iso-compositional: The simplest strategy for projecting measured mineral chemistries to higher pressures and temperatures is to merely plug the pressure and temperature of interest into the oxybarometer equation (equation 4 in Davis et al., 2017). Increasing pressure from 0.6 GPa (estimated pressure of peridotite closure conditions, based on the simplified geotherm of Montési and Behn (2007)) to 1.25 GPa (estimated source conditions for last equilibrium with basalt – the P–T of basalt/residue separation, based on the thermobarometer of Lee et al. (2009)) results in a decrease in f_{O2}. Relative to QFM at the corresponding pressures, this decrease is ∼0.30 log units for the SWIR peridotite dataset. For temperature, calculated f_{O2} is positively correlated with this

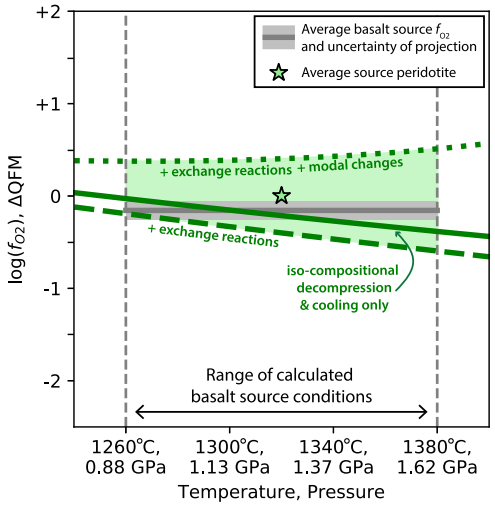

Fig. 6. Three methods for projecting peridotite f_{O2} back to source conditions. The x-axis represents the trend in pressure–temperature space that describes the calculated basalt source conditions. The gray line and field denote the average basalt f_{O2} at source conditions, plus the error associated with projection to these conditions. The green lines denote three methods of projecting peridotite to source conditions, and represent the average of the SWIR peridotite dataset, when the model is applied to each individual sample. The solid line denotes an iso-compositional projection, in which higher pressure and temperature are used in the spinel oxybarometry equation at constant mineral compositions. The long-dashed line denotes a projection that takes into account a variety of exchange reactions between minerals. The short-dashed line denotes a projection in which both exchange reactions and modal changes are considered (see text for further details on each projection method). All three projection lines converge at ∼900 °C and 0.6 GPa (the recorded closure conditions of the peridotite samples). The green shaded region denotes the range of our best estimate for the f_{O2} of source mantle as implied by peridotites. The green star is the midpoint of this shaded region and the value that we use for peridotite source conditions. Errors shown represent only the error associated with projection to source conditions, and do not include other sources of error in the calculation of f_{O2} by spinel oxybarometry or μ-XANES.

term in the oxybarometer equation, but the activity of magnetite in spinel is inversely correlated with temperature (Davis et al., 2017). As a result, increasing temperature results in an overall decrease in calculated oxygen fugacity. Projecting from ∼900 °C (closure temperature based on spinel–olivine thermometry) back to 1320 °C (estimated source conditions) results in a decrease in f_{O2}, relative to QFM at the corresponding temperatures, of ∼0.58 log units for the SWIR peridotite dataset. Thus both pressure and temperature have the same directional effect on calculated oxygen fugacity. Together, these result in a decrease of ∼0.80 log units relative to

QFM from the recorded conditions of last equilibrium to the estimated source conditions, when no other chemical changes are considered [Fig. 6].

Exchange reactions: For many elements and minerals within a peridotite, distribution coefficients are strongly dependent on temperature. For these subsystems, diffusion will occur between minerals as the peridotite cools, until the closure temperature of the system is reached (e.g., Dodson, 1973; Cherniak and Liang, 2007; Dygert and Liang, 2015). For Fe^{2+} and Mg^{2+}, both small ions with low charge, diffusion will continue to relatively low temperatures. As a result, geothermometers based on Fe^{2+}–Mg^{2+} exchange between minerals – commonly between olivine and spinel (e.g., Fabriès, 1979; O'Neill and Wall, 1987; Sack and Ghiorso, 1989, 1991a, 1991b; Li et al., 1995) – will record lower temperatures than thermometers based on less mobile elements. For instance, thermometry based on REE diffusion between pyroxenes (e.g., Liang et al., 2013) records temperatures ~200 °C higher than thermometry based on diffusion of major elements between pyroxenes (e.g., Brey and Kohler, 1990), both of which return higher temperatures than olivine-spinel thermometry for abyssal peridotites (e.g., Jaroslow et al., 1996; Dygert and Liang, 2015; Birner et al., 2017).

To assess the effect of subsolidus exchange reactions on recorded f_{O2}, we modeled both Fe^{2+}–Mg^{2+} diffusion between olivine and spinel and Al^{3+}–Cr^{3+} diffusion between spinel and orthopyroxene as a function of temperature, using the model framework put forth in Voigt and von der Handt (2011). To project our measured peridotite compositions back to the source temperature and pressure implied by basalts, we adjusted the spinel, olivine, and orthopyroxene compositions while holding bulk composition constant, until both thermometers returned the temperature of interest. This method leads to f_{O2} values that are ~0.15–0.20 log units more reduced at source temperatures and pressures than the iso-compositional method, suggesting that exchange reactions will cause peridotites to record higher f_{O2} values as subsolidus cooling proceeds [Fig. 6].

Exchange reactions and modal changes: In addition to exchange reactions, peridotites likely undergo modal changes during closed system cooling. For instance, Canil and O'Neill (1996) hypothesized that spinel may be produced at the expense of olivine and an Al-rich pyroxene component during cooling, which would then affect compositional trends for these minerals. Voigt and von der Handt (2011) included such a reaction in their subsolidus cooling model, in which spinel and Al-poor orthopyroxene are produced at the expense of olivine and Al-rich orthopyroxene as temperature decreases. If distribution of ferric iron is held constant between phases as this reaction proceeds, the content of ferric iron in spinel will be diluted as more spinel is produced, resulting in a decrease in recorded f_{O2} during cooling [Fig. 6]. However, some ferric iron is likely transferred from pyroxene to spinel during this process, which will at least partially offset this effect. A more robust understanding of the partitioning of ferric iron between spinel and pyroxene is thus needed to fully understand the subsolidus evolution of peridotites and is beyond this scope of work.

We consider the projection using exchange reactions (solid line in Fig. 6) to be a minimum value for source f_{O2} and the projection that includes modal changes (dotted line in Fig. 6) to be a maximum value for source f_{O2}. To estimate the average source f_{O2} for our peridotites, we take the midpoint between these two extremes. The midpoint may therefore be inaccurate by up to 0.5 log units based on the maximum difference between these two models in the range of basalt source conditions. Because the choice of projection scheme will shift the entire dataset upwards or downwards in f_{O2}, it does not contribute to our precision. Thus, using peridotites, we find that the MORB-source upper mantle lies at QFM 0.00, with a standard deviation of ±0.72 log units and a standard error of the mean of ±0.13 log units. The mean may be inaccurate by up to ±0.5 log units associated with the method of projection to source conditions [Table 3].

5.1.3. Agreement of peridotite and basalt oxygen fugacity at source conditions

Our projections of peridotite and basalt f_{O2} to conditions of last equilibrium between the two lithologies suggest excellent agreement between the two datasets [Fig. 7]. Our peridotite dataset suggests a source f_{O2} of QFM 0.00, with a standard error of the mean of 0.13, and with an additional error of 0.5 log units for this value depending on the method of projection to source conditions. This value is not dependent on our choice of geotherm, as the peridotite projection methods are path independent and depend only on the measured mineral compositions and the final source pressure and temperature of interest (determined from basalt source conditions calculated using the Lee et al. (2009), thermobarometer). In comparison, the basalt-derived estimate for source f_{O2} is QFM −0.16, with a standard error of the mean of 0.03. This agreement between peridotite and basalt f_{O2} at upper asthenospheric mantle conditions is consistent with the concept of basalts being produced in chemical equilibrium with residual peridotite during partial melting. Our results additionally suggest that this melting occurs at an oxygen fugacity either at or just below the QFM buffer.

Our result indicates that peridotite and basalt f_{O2} are in good agreement at SWIR and that the f_{O2} recorded by SWIR basalts is within error of the global mean from Zhang et al. (2018). The f_{O2} we calculated for SWIR peridotite PS86 D6-37 based on analysis in this study is also consistent with the f_{O2} we recalculated for PS86 D6-37 using data reported by Bryndzia and Wood (1990). The distribution of f_{O2} recorded at SWIR, however, is offset to higher f_{O2} than the distribution recorded by peridotites in the global dataset of Bryndzia and Wood (1990). If SWIR is typical of MORB mantle globally, as we would surmise from the basalt data, this raises questions about how well the Bryndzia and Wood (1990) dataset represents global peridotites. Too few mid-ocean ridge peridotites may have been measured globally to provide a representative sample of the average f_{O2} of the MORB source mantle. More work is needed to develop a more representative global ridge peridotite dataset for f_{O2}.

5.2. What factors generate heterogeneous peridotites and homogeneous basalts?

Peridotites at SWIR record a much greater range in oxygen fugacity than their basalt counterparts. Along the Oblique Segment, peridotite f_{O2} spans almost three log units, while basalt f_{O2} spans less than one. SWIR peridotite f_{O2} does not vary on the scale of a single thin section (1σ for each sample is within the error of the spinel oxybarometry method; Table 2), but f_{O2} can vary by over two log units within a single dredge. Although some of this peridotite heterogeneity may be SWIR-specific, due to influence from the nearby Bouvet hotspot (e.g., le Roex et al., 1992; Warren et al., 2009), SWIR basalt f_{O2} values are no more variable than observed at other ridge segments (e.g., Cottrell and Kelley, 2011).

The large dynamic range in f_{O2} recorded by peridotites from a single segment raises the question, what factors generate the large f_{O2} heterogeneity observed in peridotites and the relatively homogeneous f_{O2} values observed in basalts? Are these factors more related to "source"—e.g., inherent compositional heterogeneity in the upper mantle– or "process"—e.g., syn- and post-melting changes in the composition of the peridotite residue? Isotopic evidence from both peridotites and basalts suggest a heterogeneous source mantle (e.g., Salters and Dick, 2002; Cipriani et al., 2004; Liu et al.,

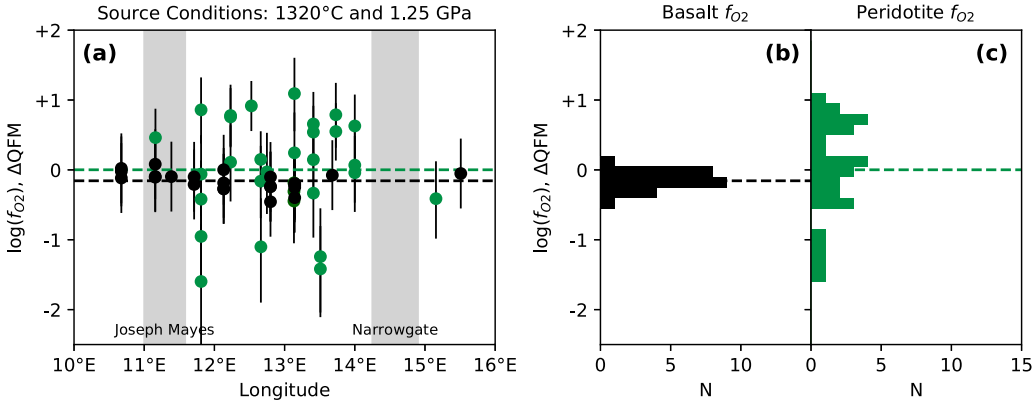

Fig. 7. (a) Oxygen fugacity results for SWIR basalts and peridotites along the axis of the Oblique Segment, projected to source conditions. Average temperature and pressure for basalts are from the thermobarometer of Lee et al. (2009), while peridotites are calculated at a value of 1320 °C and 1.25 GPa, as described in the text. For basalts, error bars represent both the error associated with the calculation of f_{O2} using the Kress and Carmichael (1991) model and the error associated with projecting each point to source conditions. For peridotites, error bars represent the uncertainty associated with the spinel oxybarometry technique for each sample, calculated using component uncertainty analysis, as described in Davis et al. (2017). The error in projection of peridotite f_{O2} to source conditions is a reflection of the accuracy of the average peridotite f_{O2} (i.e., the position of the green dashed line), as choice of projection method will shift the entire dataset in f_{O2} space. Thus, this error is not shown associated with individual points, in contrast to basalt projection errors, which are uncorrelated between individual points. **(b)** Histogram of oxygen fugacity for Oblique Segment basalts projected to source conditions. **(c)** Histogram of oxygen fugacity for Oblique Segment peridotites projected to source conditions. When projected to source conditions, peridotites and basalts record nearly identical oxygen fugacity, suggesting that these two proxies for upper mantle f_{O2} are in good agreement.

2008; Warren et al., 2009; Gale et al., 2014; Mallick et al., 2014) in which juxtaposed mantle domains of varying lithologies, ages, and tectonic/petrologic histories melt to produce MORB (e.g., Meyzen et al., 2007; Shorttle et al., 2014; Shimizu et al., 2016). In contrast, much of the major and trace element variability observed in mid-ocean ridge peridotites is driven by the process of melt extraction, as the solid residue becomes progressively depleted in incompatible elements as fractional melting proceeds (e.g., Dick et al., 1984; Johnson et al., 1990; Kinzler and Grove, 1992; Hirschmann et al., 1998), and by the process of melt–rock interaction, as these residues interact with percolating melts enriched in incompatible elements (e.g., Kelemen et al., 1992; Hellebrand et al., 2002; Brunelli et al., 2014; Warren, 2016).

Either of these two contrasting modes of mantle heterogeneity—"source" or "process"—may also control the f_{O2} heterogeneity observed in our SWIR peridotite samples. If variations in mantle source lithology or source composition exist beneath the Southwest Indian Ridge, then the heterogeneity in f_{O2} observed in SWIR peridotites could represent direct sampling of a chemically heterogeneous source mantle. In this case, more homogeneous basalt compositions suggest either that melt mixing subdues source f_{O2} variability or that MORB does not evenly sample all chemical reservoirs of the upper mantle. Alternatively, if f_{O2} under ridges is primarily controlled by the major element composition of the source mantle, then the heterogeneity seen at SWIR could potentially be induced from processes such as melting, melt–rock reaction, or thermal history rather than representing an initially heterogeneous source. In this case, more homogeneous basalt compositions derive from a source mantle relatively uniform in f_{O2}, and the peridotite heterogeneity observed at the surface is developed during partial melting and/or the solid residue's long, slow ascent to the seafloor.

A more comprehensive mid-ocean ridge peridotite dataset is needed in order to distinguish between these two hypotheses. A larger global dataset would allow for investigation of the effects of various mantle processes, such as melt extraction and melt–rock reaction, on recorded peridotite f_{O2}, as well as investigation of systematics with signatures of source heterogeneity, such as isotopes and trace elements. Regardless, our results show that, while mid-ocean ridge peridotites and basalts tell consistent stories about the average oxygen fugacity of the upper mantle, each lithology provides its own unique perspective about the nature of the upper mantle.

6. Conclusion

We investigate the oxygen fugacity of the upper mantle beneath the Southwest Indian Ridge from the perspective of both basalts and peridotites. By projecting each lithology back to source conditions, we show that peridotite f_{O2} determined by spinel oxybarometry and basalt f_{O2} determined by μ-XANES are consistent proxies for the oxygen fugacity of the asthenospheric mantle. Both lithologies record ~QFM; however, peridotites record five times the dynamic range in f_{O2}, suggesting that basalts may homogenize redox heterogeneity in the upper mantle. A larger and more comprehensive global peridotite f_{O2} dataset is needed in order to fully understand the causes of the extreme heterogeneity seen on the dredge, segment, and global scales.

Acknowledgements

We gratefully acknowledge Bernard Wood for providing the spinel calibration suite to the Smithsonian Institution. We are forever in the debt of Tim Gooding at Smithsonian for orchestrating the "prep miracle" following the 2013 government shutdown just prior to beamtime. We thank Tim Rose for laboratory support at the Smithsonian Institution and Tony Lanzirotti, Sue Wirik, and Matt Newville for their help at NSLS and GSECARS. We also thank Laurent Montési for productive conversations about the geotherm at SWIR and for providing the output for the Montési and Behn (2007) model for spreading at slow to ultraslow mid-ocean ridges. Finally, we thank Victor Kress for providing us with the raw data for the experiments used to calibrate the Kress and Carmichael (1991) model.

Funding: We gratefully acknowledge National Science Foundation the support through award OCE-1433212 (to E.C. and F.D.), OCE-1434199 and OCE-1620276 (to J.M.W.), and OCE-1433182 (to K.K.). X26A was supported by the U.S. Department of Energy (DOE) – Geosciences (DE-FG02-92ER14244 to The University of Chicago – CARS). Use of the NSLS was supported by The U.S. Department of Energy (DOE) Office of Science under Contract No. DE-AC02-98CH10886. GeoSoilEnviroCARS is supported by the National Science Foundation – Earth Sciences (EAR-1634415) and U.S. Department of Energy – GeoSciences (DE-FG02-94ER14466). Use of the Advanced Photon Source was supported by DOE Office of Science by Argonne National Laboratory under Contract No. DE-AC02-06CH11357. We additionally thank Bernard Wood and an

Table A.1
Beam session information.

	Flux density (photons/sec/μm^2)	Foil position (eV)	Beam size (μm)	Energy Min (eV)	Energy Max (eV)	Edge-step norm. (eV)
NSLS 1480	6.7×10^7	7112.049	9×5	7020	7217	7200–7217
NSLS 1514	6.7×10^7	7112.155	9×5	7020	7217	7200–7217
APS 2014_3C	3×10^6	7110.7	25×25	7040	7280	7272–7280
APS 2016_2C	8×10^6	7110.75	25×25	7012	7362	7320–7332

NSLS 1480/1514 collection conditions

	7020–7105 eV	7105–7118 eV	7118–7440 eV	7140–7220 eV
Step	10 eV	0.1 eV	1 eV	4 eV
Dwell	1 sec	5 sec	2 sec	2 sec

APS 2014_3C collection conditions

	7040–7105 eV	7105–7118 eV	7118–7280 eV
Step	5 eV	0.1 eV	0.05 Å^{-1}
Dwell	1 sec	3 sec	1 sec

APS 2016_2C collection conditions

	7012–7102 eV	7102–7132 eV	7132–7362 eV
Step	2.5 eV	0.1 eV	0.05 Å^{-1}
Dwell	1 sec	2 sec	1 sec

anonymous reviewer for their insightful feedback, and we thank Michael Bickle for editorial handing.

Appendix A. μ-XANES methodology

At the National Synchrotron Light Source I (NSLS) bending-magnet station X26a, we followed the procedures for data collection described in Cottrell et al. (2009). We collected in fluorescence mode, using a Si [311] monochrometer, over an energy range of 7020–7220 eV. The first derivative of Fe K-edge spectra (E_0) collected on zero-valent Fe is ~7112 eV. The incident beam flux was $\sim 3 \times 10^9$ photons/second with a nominal beam size of 9 μm × 5 μm, resulting in an instantaneous dose of 6.7×10^7 photons/sec/μm^2. A reference glass (LW_0) was monitored intermittently in order to assess energy drift, which occurred primarily due to thermal load on the monochrometer. This glass was run after every 5 unknowns during routine analysis and after every unknown during times of variable thermal load (for instance, after reinjection of the storage ring). Data reduction followed procedures of Cottrell et al. (2009).

For Advanced Photon Source (APS) undulator station 13-ID-E, details regarding the beamline configuration can be found in Sutton et al. (2017). The high photon flux densities delivered at undulator sources may oxidize Fe^{2+} to Fe^{3+} in hydrous basalts (Cottrell et al., 2018), thus we decreased the nominal flux from 10^{11} to $\sim 10^9$ photons/sec and defocused the beam to 25 μm × 25 μm. These conditions deliver a radiation dose similar to station X26a and decrease damage-induced oxidation to within the uncertainty and accuracy achieved through application of the Mössbauer-based anhydrous glass calibration curve (Cottrell et al., 2018).

We collected fluorescence spectra with a Vortex ME4 silicon-drift diode detector array coupled to a high-speed digital spectrometer system (Quantum Xpress3). A cryogenically cooled double-crystal Si (311) monochromator provided the monochromatic radiation. The first derivative of Fe K-edge spectra (E_0) collected on zero-valent Fe is ~7110.75 eV. We measured glass reference standard LW_0 once per every 16 unknowns as the monochrometer is liquid nitrogen cooled and we found no systematic time-dependent drift in the centroid position of this standard at the APS.

Information for each beam line session is tabulated in Table A.1.

At both facilities, we collected three spectra per sample, on a new spot each time, and visually inspected each spectrum for evidence of crystal interference. Spectra with evidence of such interference were eliminated from further analysis. Differences in the radiation sources, optics, and calibration procedures between the two synchrotron facilities change the details of the XANES spectra (Cottrell et al., 2018). We standardize results between the facilities by referencing all spectra to a standard (here, LW_0 centroid ≡ 7112.3 eV). By referencing to a standard, the calibration curve at each synchrotron station is within the precision of the technique reported by Cottrell et al. (2009). We report our precision for the centroids and $Fe^{3+}/\Sigma Fe$ ratios of the SWIR basalts in Supplemental Table 5. This reflects sample-specific reproducibility, and encompasses any sample heterogeneity. Instrumental precision on the centroid of basalt glass standard AII_-05 (Cottrell et al., 2009) is ±0.004 eV. Root mean square uncertainty on $Fe^{3+}/\Sigma Fe$ ratios predicted by our basalt calibration for unknowns is ±0.01 (Zhang et al., 2018).

Appendix B. Reassessment of Bryndzia and Wood (1990) data

B.1. Synopsis of Davis et al. (2017) methodology

Bryndzia and Wood (1990) presented a global f_{O2} dataset for 35 mid-ocean ridge peridotites based on the spinel oxybarometry method of Wood and Virgo (1989). We have re-assessed the BW90 dataset based on modifications to the spinel oxybarometry methodology presented by Davis et al. (2017). This method differs slightly from the original Wood and Virgo (1989) method in several important ways. First, the Davis et al. (2017) method uses the spinel activity model of Sack and Ghiorso (1991a, 1991b) in place of the Nell and Wood (1991) model. This model has been shown to better replicate the experimental data of Wood, 1990 (Herd, 2008; Davis et al., 2017) and is applicable to a wider range of spinel compositions (Birner et al., 2017). Although we use the Sack–Ghiorso model for the reasons outlined above, we show in Supplemental Fig. 9 that the choice of Sack–Ghiorso vs Nell–Wood spinel activity model does not affect our conclusion that basalt and peridotite f_{O2} data agree at SWIR. Second, the Davis et al. (2017) method allows the user to choose the reference buffer, whereas the Wood and Virgo (1989) equation assumes comparison to the QFM buffer parameterization of Myers and Eugster (1983). For our study, as

in Davis et al. (2017), we reference our results to the QFM buffer parameterization of Frost (1991). Finally, Davis et al. (2017) calculates the error on the spinel oxybarometry method using individual component analysis, allowing us to assess the importance of each variable to our results. Comparison of published results in Bryndzia and Wood (1990) and the results recalculated using the Davis et al. (2017) method is reported in Supplemental Table 3 and shown in Supplemental Fig. 2a, b.

B.2. The effect of using lower temperature and pressure to calculate f_{O2}

Bryndzia and Wood calculated f_{O2} at 1150 °C, the average temperature of the four locations in their data set, according to the two-pyroxene thermometer of Wells (1977). We have chosen to apply the olivine-spinel Fe^{2+}–Mg^{2+} exchange thermometer of Li et al. (1995), which records lower temperatures (average ~900 °C) as diffusion of Fe^{2+} and Mg^{2+} continues to lower temperatures. The spinel oxybarometry equation is highly dependent on the Mg/Fe content of both olivine (through the calculation of $a_{Fe2SiO4}$) and spinel (through the calculation of a_{Fe3O4}). Hence, we consider this thermometer to be the most representative of f_{O2} closure conditions (e.g., Birner et al., 2017), although significantly lower than the temperature of last equilibrium with basalt (1260–1380 °C, based on the Lee et al., 2009, thermobarometer results for basalts in this study). Temperatures for the 11 Bryndzia and Wood samples with measured olivine average 948 ± 44 °C [Supplemental Table 3], compared to an average temperature of 899 ± 59 °C for SWIR peridotites in this study. Bryndzia and Wood (1990) referenced their data to 1 GPa based on the center of the spinel stability field and the conditions under which MORBs have been found experimentally to be in equilibrium with spinel lherzolite. However, we choose a lower pressure of 0.6 GPa to match the calculated temperatures, using a thermal model derived from Montési and Behn (2007; see main text section 3.5 for more detail) for the SWIR Oblique Segment. We expect this pressure to be broadly applicable to the Bryndzia and Wood (1990) samples as well, as 21 out of their 33 samples are from similarly slow-spreading ridges and pressure has a relatively small effect on calculated f_{O2} (e.g., Davis et al., 2017). Additionally, while 1 GPa has traditionally been considered the lower pressure limit for spinel stability, experiments by Borghini et al. (2010) show that chrome-bearing spinel is stable to pressures of 0.6 GPa and coexists with plagioclase to even lower pressures. All but one of our samples has a higher Cr content than the most Cr-rich spinel analyzed in Borghini et al. (2010), and as more Cr-rich compositions are expected to stabilize spinel to progressively lower pressures, the spinels in our study were stable to at least 0.6 GPa. This is consistent with the petrographic observation that plagioclase is absent in the majority of abyssal peridotites (Warren, 2016). Results for the Bryndzia and Wood (1990) dataset recalculated using olivine-spinel thermometry and a pressure of 0.6 GPa are shown in Fig. 4c and Supplemental Fig. 2c and are reported in Supplemental Table 3.

B.3. Assessment of error introduced when olivine and orthopyroxene compositional data are not available

For 24 of the 35 samples reported in Bryndzia and Wood (1990), major element compositions for olivine and orthopyroxene are not available. As these values are needed for the calculation of f_{O2}, we assess the error that is introduced by assuming a 'typical' ridge value for these parameters. Orthopyroxene affects f_{O2} through the parameter $a_{Fe2Si2O6}$, whereas olivine composition is used to calculate $a_{Fe2SiO4}$ and temperature, which in turn affects calculated a_{Fe3O4}. In order to propagate total error through the f_{O2} equation, we performed a Monte Carlo analysis for each of the 24 samples missing olivine and orthopyroxene data following these steps:

1. We determined a probability density function for Fo# based on the distribution of Fo# in all ridge peridotites from the global dataset of Warren (2016). The histogram of Fo# values and the resultant probability density function are shown in Supplemental Fig. 3a.
2. We performed a linear regression on $X^{M1}X^{M2}$ in opx and Fo# in olivine for all 293 global ridge peridotites for which both minerals have been measured (Supplemental Fig. 3b). These two parameters are correlated ($R^2 = 0.62$) in ridge peridotites, and the linear regression has a standard error of 0.00058 for estimation of $X^{M1}X^{M2}$ in opx (Supplemental Fig. 3b).
3. We generated 1000 Fo# values for each sample using the probability density function determined in step (1).
4. We generated a $X^{M1}X^{M2}$ value corresponding to each Fo#. This was done by choosing a random value from a normal distribution with a mean determined by the linear regression in step (2) and a standard deviation determined by the standard error of the linear regression.
5. We calculated temperature and f_{O2} for each generated condition, using the generated Fo# and $X^{M1}X^{M2}$ values in conjunction with the reported spinel composition for each sample.
6. Finally, we determined the mean and standard deviation of the 1000 f_{O2} values generated for each sample, in order to assess the variation in f_{O2} introduced by the lack of data for olivine and orthopyroxene. Errors derived from other sources were calculated as normal, using the method of Davis et al. (2017).

Supplemental Fig. 3c shows the average f_{O2} results for each sample determined from the Monte Carlo simulation (light green histogram), in conjunction with samples for which olivine and orthopyroxene data were reported (dark green histogram). Samples without olivine and pyroxene data have ~0.15 log units of additional uncertainty compared to samples with olivine and orthopyroxene compositions, as shown in the figure. This added uncertainty is relatively small compared to the total error in f_{O2} for a given sample and compared to the f_{O2} range of the Bryndzia and Wood (1990) samples. Therefore, we conclude that samples missing olivine and orthopyroxene data can be included when comparing the Bryndzia and Wood (1990) results to our SWIR results. We use this method when recalculating f_{O2} values for the Bryndzia and Wood (1990) samples missing olivine and orthopyroxene [Supplemental Table 3; Fig. 4c; Supplemental Fig. 2b, c].

We do, however, exclude samples from St. Paul's Rocks and the Mid-Cayman Rise. Samples from St. Paul's Rocks were excluded by Bryndzia and Wood (1990) as they are unusual, sub-aerially exposed, amphibole-bearing mylonites. We additionally exclude samples from the Mid-Cayman Spreading Center, which is a complex tectonic setting due to nearby subducting slabs (e.g., Hayman et al., 2011). However, the Mid-Cayman samples record fairly typical f_{O2} values, so exclusion of these samples does not affect the overall systematics of the Bryndzia and Wood (1990) sample set.

Appendix C. Calculation of source f_{O2} for basalts

C.1. Fractional crystallization correction

As a parcel of magma cools, its composition will be altered by the crystallization of phases with high melting points, such as olivine and pyroxene. The effect of fractional crystallization on magma composition can be corrected for by regressing each major element oxide to a constant wt% MgO value along empirical, segment-specific liquid lines of descent (LLDs; e.g. Klein and Langmuir, 1987). We determined empirical LLDs for each section of the Oblique Segment using all Oblique Segment glasses with major element compositions reported in the Volcanic Glass Reference File

(Melson et al., 2002;[1] $n = 175$; Supplemental Figs. 4–5). For this study, we corrected our samples along these empirical LLDs back to 8.5 wt% MgO, at which point olivine should be the only phase on the liquidus. The LLDs for the Oblique sections 1, 2, and 3 are linear, whereas the LLDs for Joseph Mayes Seamount have a distinct kink, likely resulting from the onset of clinopyroxene fractionation.

Because $Fe^{3+}/\Sigma Fe$ data are available only for samples from this study and not for the whole of the Oblique Segment major element dataset, the correlation between $Fe^{3+}/\Sigma Fe$ and MgO is less well constrained than for the major element oxides. When choosing a correction slope, we considered the global distribution of MORB for which $Fe^{3+}/\Sigma Fe$ and MgO are known, the theoretical slope of olivine fractionation, and the distribution of our samples. The global dataset has a slope close to −0.005, while the olivine fractionation slope is slightly curved and varies from −0.005 to −0.006 over the range of MgO values investigated in this study. For the SWIR samples, the slope is closer to −0.008 (excluding Narrowgate samples; see next paragraph), although this slope is dominated by one reduced sample at high MgO content. When this sample is excluded, the slope is closer to −0.006. As shown in Supplemental Fig. 7, the choice of slope makes relatively little difference for a basalt fractionating over the range of MgO = 6 wt% to MgO = 8.5 wt%. Overall, we chose −0.006 as our correction slope and include a standard error of 0.002 when calculating the error associated with projection of basalt to source conditions (see Appendix C.5 for more details on error calculation).

For samples from Narrowgate, the liquid lines of descent are not well defined at MgO contents greater than 7.5 wt% [Supplemental Fig. 6], due to a paucity of samples at high MgO content. As a result, we cannot determine whether Narrowgate LLDs have a kink at high MgO content, as seen in the Joseph Mayes Seamount data [Supplemental Fig. 5]. For instance, extrapolating the Narrowgate trend for FeO* to high MgO leads to extremely low FeO* contents of ∼6 wt%, whereas a kink could bring the values up to as high as 9 or 10 wt%, if the high MgO trend follows the same slope as the Joseph Mayes high MgO trend. This difference affects the pressure and temperature of equilibrium, as well as calculated oxygen fugacity. As a result, we have excluded the Narrowgate samples from our calculation of source f_{O2}.

C.2. Reverse crystallization of olivine to equilibrium with Fo90

To determine the primary magma composition for each of our samples, we made the assumption that only olivine is on the liquidus at MgO contents greater than 8.5 wt%. We then calculated the forsterite content of olivine in equilibrium with the fractional crystallization corrected compositions using $K_D{}^{Mg-Fe}$ Ol-Liq = 0.3, added incremental olivine of that composition back into the melt, and iterated this process until equilibrium with Fo90 was reached. These new compositions range from ∼9.5–13.0 wt% MgO [Supplemental Table 10], with the samples from Joseph Mayes Seamount recording the highest MgO contents at equilibrium with Fo90.

C.3. Determination of pressure and temperature of basalt at source conditions

The reconstructed compositions determined in Appendix C.2 are representative of the composition of the primary magma at the time of extraction from the mantle. This corresponds to the time of last equilibrium between the basaltic melt and its peridotite residue. To determine the pressure and temperature of this last equilibrium, we used the thermobarometer of Lee et al. (2009). Calculated temperatures for the basalt glasses range from ∼1260–1380 °C, at corresponding pressures of ∼0.9–1.7 GPa. Pressures and temperatures are well correlated ($R^2 = 0.96$) and the maximum temperature of 1380 °C is in good agreement with the potential temperature estimate of 1350–1380 °C for the Oblique Segment (Dalton et al., 2014). Temperatures and pressures for the Joseph Mayes Seamount are higher than those for the Oblique 1, 2, and 3 sections [Table 1], suggesting a deeper last equilibration with peridotite for these samples. To determine the best estimate for source pressure and temperature, which we use later to project peridotites to source conditions, we took the middle of the temperature range (1320 °C) and used the correlation between pressure and temperature ($P = 0.0061*T - 6.82$) to choose a corresponding pressure of 1.25 GPa. Notably, these represent deeper conditions than recorded by peridotites [e.g., Table 2], indicating that peridotites have undergone subsolidus reequilibration since their last equilibrium with basaltic magmas at source conditions.

Table A.1
Monte Carlo error inputs.

Source of error	Error estimate (1σ)
Fo content of mantle residue	±1
Primitive MgO content	±0.5
Slope of fractional crystallization correction lines for each oxide	±10%
Slope of $Fe^{3+}/\Sigma Fe$ fractional crystallization correction line	±0.002
Oxide errors for EPMA data:	
Al_2O_3	±0.05%
FeO*	±1%
CaO	±3%
Na_2O	±2%
K_2O	±5%
Determination of $Fe^{3+}/\Sigma Fe$ by μ-XANES	±3%
Pressure and temperature calculated from Lee et al. (2009)	±20%

C.4. Determination of f_{O2} of basalt at source conditions

We calculated the f_{O2} of the basalt samples at the conditions of last equilibrium based on the P–T conditions determined in Appendix C.3 [Supplemental Table 10; Table 1]. We used the formulation of Kress and Carmichael (1991) and the primary magma compositions calculated in Appendix C.2. Calculated source f_{O2} values average -0.16 ± 0.13, with no difference between samples from Joseph Mayes Seamount compared to the Oblique 1, 2, and 3 sections. Additionally, we see no trend between calculated temperature/pressure and source f_{O2} relative to QFM ($R^2 = 0.05$).

C.5. Error estimates

To determine the total uncertainty in the source f_{O2} values calculated for the Oblique Segment basalts, we estimated the error associated with each individual step above and applied a Monte Carlo simulation ($N = 1000$). We took the error associated with each step from Brounce et al. (2014) with the exception of the error on the slope of the $Fe^{3+}/\Sigma Fe$ fractional crystallization correction line [Supplemental Fig. 7]. Table A.1 summarizes the individual errors, where values listed as percentages are relative to the measured/calculated value, while other values are absolute magnitudes of error.

Our Monte Carlo analysis suggests that the total error associated with projecting the SWIR basalts to source conditions is ∼0.12 log units. Comparatively, the standard error associated with

[1] In our investigation of basalt major element compositions, we found discrepancies between the values listed in the Volcanic Glass data file and those published in Standish et al. (2008). Based on re-measurement of one of the glasses with conflicting data, we believe that the values in the Volcanic Glass data file are correct, and have used these values throughout this study.

the Kress and Carmichael (1991) formulation for calculating f_{O2} from composition, pressure, and temperature is 0.35 log units for MORB glasses [Supplemental Fig. 8].

Appendix D. Projection of peridotites to source conditions

To calculate the f_{O2} of basalt-source mantle as implied by peridotites, we projected the peridotite compositions to the source pressure–temperature conditions implied by the basalts Appendix C.3. We used the framework of Voigt and von der Handt (2011) in conjunction with the following reactions:

1. Fe^{2+}–Mg^{2+} exchange between olivine and spinel:

$$Fe_2SiO_4(ol) + 2MgAl_2O_4(sp) \leftrightarrow Mg_2SiO_4(ol) + 2FeAl_2O_4(sp) \quad (D.1a)$$

We use the thermometer of Li et al. (1995) for this reaction:

$$T_{sp/ol} = \frac{4299Y_{Cr} + 1283}{\ln K_D^{sp/ol} - 2Y_{Fe^{3+}} + 1.469Y_{Cr} + 0.363} - 273.15 \quad (D.1b)$$

2. Cr^{3+}–Al^{3+} exchange between spinel and orthopyroxene:

$$MgAl_2SiO_6(opx) + MgCr_2O_4(sp) \leftrightarrow MgCr_2SiO_6(opx) + MgAl_2O_4(sp) \quad (D.2a)$$

We use the thermometer of Witt-Eickschen and O'Neill (2005) for this reaction:

$$T_{opx/sp} = \frac{1215 + 3137Cr\#^{sp}}{\ln K_D^{opx/sp} + 0.391} - 273.15 \quad (D.2b)$$

3. Tschermak exchange in orthopyroxene:

$$MgAl_2O_4(sp) + Mg_2Si_2O_6(opx) \leftrightarrow Mg_2SiO_4(ol) + MgAl_2SiO_6(opx) \quad (D.3a)$$

We use the thermometer of Voigt and von der Handt (2011) for this reaction:

$$T_{Ts\text{-}opx} = 2248.25 + 991.58\ln K_D^{Ts\text{-}opx} + 153.32\left(\ln K_D^{Ts\text{-}opx}\right)^2 + 539.05Cr\#^{sp} - 2005.74\left(Cr\#^{sp}\right)^2 \quad (D.3b)$$

To determine the composition of each projected peridotite, we assign each reaction a variable, P, representing the progress of that reaction to get from recorded conditions to projected conditions (e.g., $P_{ol/sp} = 2$ would mean that 2 moles of Fe_2SiO_4 and 4 moles of $MgAl_2O_4$ are added to the measured compositions, while 2 moles of Mg_2SiO_4 and 4 moles of $FeAl_2O_4$ are subtracted). We then set up a system of equations that varies $P_{ol/sp}$, $P_{opx/sp}$, and $P_{Ts\text{-}opx}$ until $T_{desired} = T_{ol/sp} = T_{opx/sp} = T_{Ts\text{-}opx}$. For our modeling, we set initial modal abundances (prior to projection) to $X_{ol} = 0.68$, $X_{opx} = 0.20$, $X_{cpx} = 0.10$, $X_{sp} = 0.02$, consistent with a relatively fertile peridotite (e.g., Warren, 2016). When only exchange reactions are considered, reactions (D.1a) and (D.2a) are used in the model; when exchange reactions and modal changes are considered, reactions (D.1a), (D.2a), and (D.3a) are used.

In order to compare our results to the global dataset of Bryndzia and Wood (1990), we additionally project the subset of their samples for which olivine and orthopyroxene data are reported ($n = 11$). Samples without olivine or orthopyroxene data cannot be projected, as the thermometry equations depend on parameters calculated from these minerals [Equations (D.1b), (D.2b), (D.3b)]. Because the conditions of last equilibration with basalt are not known for these samples, we compare the datasets at the pressure and temperature conditions calculated for SWIR (1320 °C and 1.25 GPa). We find that the projectable subset of Bryndzia and Wood (1990) peridotites record lower f_{O2}, on average, than the SWIR peridotites from this study at both recorded and projected conditions [Supplemental Fig. 10]. The four most reduced samples from the Bryndzia and Wood (1990) dataset are peridotites dredged from the Islas Orcadas Fracture Zone. These results suggest that the average oxygen fugacity of sub-ridge mantle may vary between ridge segments. Further sampling and analytical work is needed in order to determine both the extent and causes of variations in oxygen fugacity between mid-ocean ridge segments.

Appendix E. Supplementary material

Supplementary material related to this article can be found online at https://doi.org/10.1016/j.epsl.2018.04.035.

References

Bézos, A., Humler, E., 2005. The $Fe^{3+}/\Sigma Fe$ ratios of MORB glasses and their implications for mantle melting. Geochim. Cosmochim. Acta 69, 711–725. https://doi.org/10.1016/j.gca.2004.07.026.

Birner, S.K., Warren, J.M., Cottrell, E., Davis, F.A., 2016. Hydrothermal alteration of seafloor peridotites does not influence oxygen fugacity recorded by spinel oxybarometry. Geology 44, G38113.1. https://doi.org/10.1130/G38113.1.

Birner, S.K., Warren, J.M., Cottrell, E., Davis, F.A., Kelley, K.A., Falloon, T.J., 2017. Forearc peridotites from Tonga record heterogeneous oxidation of the mantle following subduction initiation. J. Petrol. 58, 1755–1780. https://doi.org/10.1093/petrology/egx072.

Borghini, G., Fumagalli, P., Rampone, E., 2010. The stability of plagioclase in the upper mantle: subsolidus experiments on fertile and depleted lherzolite. J. Petrol. 51, 229–254. https://doi.org/10.1093/petrology/egp079.

Brey, G.P., Kohler, T., 1990. Geothermobarometry in four-phase lherzolites II. New thermobarometers, and practical assessment of existing thermobarometers. J. Petrol. 31, 1353–1378.

Brounce, M.N., Kelley, K.A., Cottrell, E., 2014. Variations in $Fe^{3+}/\Sigma Fe$ of Mariana arc basalts and mantle wedge fO_2. J. Petrol. 55, 2513–2536.

Brounce, M., Stolper, E., Eiler, J., 2017. Redox variations in Mauna Kea lavas, the oxygen fugacity of the Hawaiian plume, and the role of volcanic gases in Earth's oxygenation. Proc. Natl. Acad. Sci. USA 114, 8997–9002. https://doi.org/10.1073/pnas.1619527114.

Brunelli, D., Paganelli, E., Seyler, M., 2014. Reactive percolation of enriched melts in the spinel-field melting region: a REE approach to abyssal peridotites from the South West Indian Ridge. Geochim. Cosmochim. Acta 127, 190–203.

Bryndzia, L.T., Wood, B.J., 1990. Oxygen thermobarometry of abyssal spinel peridotites: the redox state and C–O–H volatile composition of the Earth's sub-oceanic upper mantle. Am. J. Sci. 290, 1093–1116. https://doi.org/10.2475/ajs.290.10.1093.

Canil, D., 1997. Vanadium partitioning and the oxidation state of Archaean komatiite magmas. Nature 389, 23–26.

Canil, D., O'Neill, H.S.C., 1996. Distribution of ferric iron in some upper-mantle assemblages. J. Petrol. 37, 609–635. https://doi.org/10.1093/petrology/37.3.609.

Cannat, M., 1996. How thick is the magmatic crust at slow spreading oceanic ridges? Melt migration in the axial lithosphere of slow spreading ridges: constraints from ultramafic and gabbroic samples. J. Geophys. Res. 101, 2847–2857.

Cannat, M., Sauter, D., Bezos, A., Meyzen, C., Humler, E., Le Rigoleur, M., 2008. Spreading rate, spreading obliquity, and melt supply at the ultraslow spreading Southwest Indian Ridge. Geochem. Geophys. Geosyst. 9, 1–26.

Carmichael, I.S.E., 1991. The redox states of basic and silicic magmas: a reflection of their source regions? Contrib. Mineral. Petrol. 106, 129–141. https://doi.org/10.1007/BF00306429.

Cherniak, D.J., Liang, Y., 2007. Rare earth element diffusion in natural enstatite. Geochim. Cosmochim. Acta 71, 1324–1340. https://doi.org/10.1016/j.gca.2006.12.001.

Christie, D.M., Carmichael, I.S.E., Langmuir, C.H., 1986. Oxidation states of mid-ocean ridge basalt glasses. Earth Planet. Sci. Lett. 79, 397–411. https://doi.org/10.1016/0012-821X(86)90195-0.

Cipriani, A., Brueckner, H.K., Bonatti, E., Brunelli, D., 2004. Oceanic crust generated by elusive parents: Sr and Nd isotopes in basalt–peridotite pairs from the Mid-Atlantic ridge. Geology 32, 657–660. https://doi.org/10.1130/G20560.1.

Cottrell, E., Kelley, K.A., 2013. Redox heterogeneity in mid-ocean ridge basalts as a function of mantle source. Science 340, 1314–1317. https://doi.org/10.1126/science.1233299.

Cottrell, E., Kelley, K.A., 2011. The oxidation state of Fe in MORB glasses and the oxygen fugacity of the upper mantle. Earth Planet. Sci. Lett. 305, 270–282. https://doi.org/10.1016/j.epsl.2011.03.014.

Cottrell, E., Kelley, K.A., Lanzirotti, A., Fischer, R.A., 2009. High-precision determination of iron oxidation state in silicate glasses using XANES. Chem. Geol. 268, 167–179. https://doi.org/10.1016/j.chemgeo.2009.08.008.

Cottrell, E., Lanzirotti, A., Mysen, B., Birner, S.K., Kelley, K.A., Botcharnikov, R., Davis, F.A., Newville, M., 2018. A Mössbauer-based XANES calibration for hydrous basalt glasses reveals radiation-induced oxidation of Fe. Am. Mineral. https://doi.org/10.2138/am-2018-6268.

Dalton, C.A., Langmuir, C.H., Gale, A., 2014. Geophysical and geochemical evidence for deep temperature variations beneath mid-ocean ridges. Science 344, 80–83. https://doi.org/10.1126/science.1249466.

Dasgupta, R., Hirschmann, M.M., 2006. Melting in the Earth's deep upper mantle caused by carbon dioxide. Nature 440, 659–662. https://doi.org/10.1038/nature04612.

Davis, F.A., Cottrell, E., Birner, S.K., Warren, J.M., Lopez, O.G., 2017. Revisiting the electron microprobe method of spinel–olivine–orthopyroxene oxybarometry applied to spinel peridotites. Am. Mineral. 102, 421–435.

Davis, F.A., Cottrell, E., in press. Experimental investigation of basalt and peridotite oxybarometers: implications for spinel thermodynamic models and Fe^{3+} compatibility during generation of upper mantle melts. Am. Mineral. https://doi.org/10.2138/am-2018-6280.

Dick, H.J.B., 1989. Abyssal peridotites, very slow spreading ridges and ocean ridge magmatism. Geol. Soc. (Lond.) Spec. Publ. 42, 71–105.

Dick, H.J.B., Fisher, R.L., Bryan, W.B., 1984. Mineralogic variability of the uppermost mantle along mid-ocean ridges. Earth Planet. Sci. Lett. 69, 88–106. https://doi.org/10.1016/0012-821X(84)90076-1.

Dick, H.J.B., Lin, J., Schouten, H., 2003. An ultraslow-spreading class of ocean ridge. Nature 426, 405–412. https://doi.org/10.1038/nature02128.

Dodson, M.H., 1973. Closure temperature in cooling geochronological and petrological systems. Contrib. Mineral. Petrol. 40, 259–274. https://doi.org/10.1007/BF00373790.

Dygert, N., Liang, Y., 2015. Temperatures and cooling rates recorded in REE in coexisting pyroxenes in ophiolitic and abyssal peridotites. Earth Planet. Sci. Lett. 420, 151–161.

Fabriès, J., 1979. Spinel–olivine geothermometry in peridotites from ultramafic complexes. Contrib. Mineral. Petrol. 69, 329–336. https://doi.org/10.1007/BF00372258.

Frost, B.R., 1991. Introduction to oxygen fugacity and its petrologic importance. Rev. Mineral. Geochem. 25, 1–9.

Frost, D.J., McCammon, C.A., 2008. The redox state of Earth's mantle. Annu. Rev. Earth Planet. Sci. 36, 389–420. https://doi.org/10.1146/annurev.earth.36.031207.124322.

Gaillard, F., Scaillet, B., Arndt, N.T., 2011. Atmospheric oxygenation caused by a change in volcanic degassing pressure. Nature 478, 229–232.

Gaillard, F., Scaillet, B., Pichavant, M., Iacono-Marziano, G., 2015. The redox geodynamics linking basalts and their mantle sources through space and time. Chem. Geol. 418, 217–233. https://doi.org/10.1016/j.chemgeo.2015.07.030.

Gale, A., Langmuir, C.H., Dalton, C.A., 2014. The global systematics of ocean ridge basalts and their origin. J. Petrol. 55, 1051–1082. https://doi.org/10.1093/petrology/egu017.

Hayman, N.W., Grindlay, N.R., Perfit, M.R., Mann, P., Leroy, S., De Lépinay, B.M., 2011. Oceanic core complex development at the ultraslow spreading Mid-Cayman Spreading Center. Geochem. Geophys. Geosyst. 12, 1–21. https://doi.org/10.1029/2010GC003240.

Hellebrand, E., Snow, J.E., Hoppe, P., Hofmann, A.W., 2002. Garnet-field melting and late-stage refertilization in "residual" abyssal peridotites from the Central Indian Ridge. J. Petrol. 43, 2305–2338. https://doi.org/10.1093/petrology/43.12.2305.

Herd, C.D.K., 2008. Basalts as probes of planetary interior redox state. Rev. Mineral. Geochem. 68, 527–553. https://doi.org/10.2138/rmg.2008.68.19.

Herzberg, C.T., Asimow, P.D., 2015. PRIMELT3 MEGA.XLSM software for primary magma calculation: peridotite primary magma MgO contents from the liquidus to the solidus. Geochem. Geophys. Geosyst. 16, 563–578. https://doi.org/10.1002/2014GC005631.Received.

Hirschmann, M.M., Ghiorso, M.S., Wasylenki, L.E., Asimow, P.D., Stolper, E.M., 1998. Calculation of peridotite partial melting from thermodynamic models of minerals and melts. I. Review of methods and comparison with experiments. J. Petrol. 39, 1091–1115. https://doi.org/10.1093/petroj/39.6.1091.

Jaroslow, G.E., Hirth, G., Dick, H.J.B., 1996. Abyssal peridotite mylonites: implications for grain-size sensitive flow and strain localization in the oceanic lithosphere. Tectonophysics 256, 17–37.

Johnson, K.T.M., Dick, H.J.B., Shimizu, N., 1990. Melting in the oceanic upper mantle: an ion microprobe study of diopsides in abyssal peridotites. J. Geophys. Res. 95, 2661. https://doi.org/10.1029/JB095iB03p02661.

Kelemen, P., Dick, H., Quick, J., 1992. Formation of harzburgite by pervasive melt/rock reaction in the upper mantle. Nature 358, 635–641.

Kelley, K.A., Cottrell, E., 2009. Water and the oxidation state of subduction zone magmas. Science 325, 605–607. https://doi.org/10.1126/science.1174156.

Kinzler, R.J., Grove, T.L., 1992. Primary magmas of mid-ocean ridge basalts: 2. Applications. J. Geophys. Res. 97, 6907–6926.

Klein, E.M., Langmuir, C.H., 1987. Global correlations of ocean ridge basalt chemistry with axial depth and crustal thickness. J. Geophys. Res. 92, 8089. https://doi.org/10.1029/JB092iB08p08089.

Kress, V.C., Carmichael, I.S.E., 1991. The compressibility of silicate liquids containing Fe_2O_3 and the effect of composition, temperature, oxygen fugacity and pressure on their redox states. Contrib. Mineral. Petrol. 108, 82–92. https://doi.org/10.1007/BF00307328.

Kushiro, I., 1968. Compositions of magmas formed by partial zone melting of the Earth's upper mantle. J. Geophys. Res. 73, 619–634. https://doi.org/10.1029/JB073i002p00619.

le Roex, A.P., Dick, H.J.B., Watkins, R.T., 1992. Petrogenesis of anomalous K-enriched MORB from the Southwest Indian Ridge: 11°53′E to 14°38′E. Contrib. Mineral. Petrol. 110, 253–268. https://doi.org/10.1007/BF00310742.

Lee, C.-T.A., Luffi, P., Plank, T., Dalton, H., Leeman, W.P., 2009. Constraints on the depths and temperatures of basaltic magma generation on Earth and other terrestrial planets using new thermobarometers for mafic magmas. Earth Planet. Sci. Lett. 279, 20–33. https://doi.org/10.1016/j.epsl.2008.12.020.

Li, J., Kornprobst, J., Vielzeuf, D., Fabriès, J., 1995. An improved experimental calibration of the olivine-spinel geothermometer. Chin. J. Geochem. 14, 68–77. https://doi.org/10.1007/BF02840385.

Liang, Y., Sun, C., Yao, L., 2013. A REE-in-two-pyroxene thermometer for mafic and ultramafic rocks. Geochim. Cosmochim. Acta 102, 246–260.

Liu, C.-Z., Snow, J.E., Hellebrand, E., Brügmann, G., von der Handt, A., Büchl, A., Hofmann, A.W., 2008. Ancient, highly heterogeneous mantle beneath Gakkel ridge, Arctic Ocean. Nature 452, 311–316. https://doi.org/10.1038/nature06688.

Mallick, S., Dick, H.J.B., Sachi-Kocher, A., Salters, V.J.M., 2014. Isotope and trace element insights into heterogeneity of subridge mantle. Geochem. Geophys. Geosyst. 15, 2438–2453.

Mattioli, G.S., Wood, B.J., 1988. Magnetite activities across the $MgAl_2O_4$–Fe_3O_4 spinel join, with application to thermobarometric estimates of upper mantle oxygen fugacity. Contrib. Mineral. Petrol. 98, 148–162.

Melson, W.G., O'Hearn, T., Jarosewich, E., 2002. A data brief on the Smithsonian abyssal volcanic glass data file. Geochem. Geophys. Geosyst. 3, 1–11. https://doi.org/10.1029/2001GC000249.

Meyzen, C.M., Blichert-Toft, J., Ludden, J.N., Humler, E., Meval, C., Albarede, F., 2007. Isotopic portrayal of the Earth's upper mantle flow field. Nature 447, 1069–1074. https://doi.org/10.1038/nature05920.

Montési, L.G.J., Behn, M.D., 2007. Mantle flow and melting underneath oblique and ultraslow mid-ocean ridges. Geophys. Res. Lett. 34, 1–5. https://doi.org/10.1029/2007GL031067.

Montési, L.G.J., Behn, M.D., Hebert, L.B., Lin, J., Barry, J.L., 2011. Controls on melt migration and extraction at the ultraslow Southwest Indian Ridge 10°–16°E. J. Geophys. Res. 116, B10102. https://doi.org/10.1029/2011JB008259.

Myers, J., Eugster, H.P., 1983. The system Fe–Si–O: oxygen buffer calibrations to 1500 K. Contrib. Mineral. Petrol. 82, 75–90. https://doi.org/10.1007/BF00371177.

Nell, J., Wood, B.J., 1991. High-temperature electrical measurements and thermodynamic properties of Fe_3O_4–$FeCr_2O_4$–$MgCr_2O_4$–$FeAl_2O_4$ spinels. Am. Mineral. 76, 405–426.

O'Neill, H.S.C., Wall, V.J., 1987. The olivine-orthopyroxene-spinel oxygen geobarometer, the nickel precipitation curve, and the oxygen fugacity of the Earth's upper mantle. J. Petrol. 28, 1169–1191.

Putirka, K.D., 2016. Rates and styles of planetary cooling on Earth, Moon, Mars, and Vesta, using new models for oxygen fugacity, ferric-ferrous ratios, olivine-liquid Fe–Mg exchange, and mantle potential temperature. Am. Mineral. 101, 819–840.

Ryan, W.B.F., Carbotte, S.M., Coplan, J.O., O'Hara, S., Melkonian, A., Arko, R., Weissel, R.A., Ferrini, V., Goodwillie, A., Nitsche, F., Bonczkowski, J., Zemsky, R., 2009. Global multi-resolution topography synthesis. Geochem. Geophys. Geosyst. 10, 1–9. https://doi.org/10.1029/2008GC002332.

Sack, R.O., Ghiorso, M.S., 1989. Importance of considerations of mixing properties in establishing an internally consistent thermodynamic database: thermochemistry of minerals in the system Mg_2SiO_4–Fe_2SiO_4–SiO_2. Contrib. Mineral. Petrol. 102, 41–68.

Sack, R.O., Ghiorso, M.S., 1991a. An internally consistent model for the thermodynamic properties of Fe–Mg-titanomagnetite-aluminate spinels. Contrib. Mineral. Petrol. 106, 474–505. https://doi.org/10.1007/BF00321989.

Sack, R.O., Ghiorso, M.S., 1991b. Chromian spinels as petrogenetic indicators: thermodynamics and petrological applications. Am. Mineral. 76, 827–847.

Salters, V.J.M., Dick, H.J.B., 2002. Mineralogy of the mid-ocean-ridge basalt source from neodymium isotopic composition of abyssal peridotites. Nature 418, 68–72. https://doi.org/10.1038/nature00886.1.

Sclater, J.G., Fisher, R.L., Patriat, P., Tapscott, C., Parsons, B., 1981. Eocene to recent development of the South-west Indian Ridge, a consequence of the evolution of the Indian Ocean Triple Junction. Geophys. J. R. Astron. Soc. 64, 587–604.

Shimizu, K., Saal, A.E., Myers, C.M., Nagle, A.N., Hauri, E.H., Forsyth, D.W., Kamenetsky, V.S., Niu, Y., 2016. Two-component mantle melting–mixing model for the generation of mid-ocean ridge basalts: implications for the volatile content of the Pacific upper mantle. Geochim. Cosmochim. Acta 176, 44–80. https://doi.org/10.1016/j.gca.2015.10.033.

Shorttle, O., Maclennan, J., Lambart, S., 2014. Quantifying lithological variability in the mantle. Earth Planet. Sci. Lett. 395, 24–40. https://doi.org/10.1016/j.epsl.2014.03.040.

Spiegelman, M., McKenzie, D., 1987. Simple 2-D models for melt extraction at mid-ocean ridges and island arcs. Earth Planet. Sci. Lett. 83, 137–152. https://doi.org/10.1016/0012-821X(87)90057-4.

Stagno, V., Ojwang, D.O., McCammon, C.A., Frost, D.J., 2013. The oxidation state of the mantle and the extraction of carbon from Earth's interior. Nature 493, 84–88. https://doi.org/10.1038/nature11679.

Standish, J.J., Dick, H.J.B., Michael, P.J., Melson, W.G., O'Hearn, T., 2008. MORB generation beneath the ultraslow spreading Southwest Indian Ridge (9–25° E): major element chemistry and the importance of process versus source. Geochem. Geophys. Geosyst. 9. https://doi.org/10.1029/2008GC001959.

Stolper, E.M., 1980. A phase diagram for Mid-Ocean Ridge basalts: preliminary results and implications for petrogenesis. Contrib. Mineral. Petrol. 74, 13–27.

Sutton, S.R., Lanzirotti, A., Newville, M., Rivers, M.L., Eng, P., Lefticariu, L., 2017. Spatially resolved elemental analysis, spectroscopy and diffraction at the GSECARS sector at the Advanced Photon Source. J. Environ. Qual. 46, 1158–1165. https://doi.org/10.2134/jeq2016.10.0401.

Voigt, M., von der Handt, A., 2011. Influence of subsolidus processes on the chromium number in spinel in ultramafic rocks. Contrib. Mineral. Petrol. 162, 675–689. https://doi.org/10.1007/s00410-011-0618-3.

Warren, J.M., Shimizu, N., Sakaguchi, C., Dick, H.J.B., Nakamura, E., 2009. An assessment of upper mantle heterogeneity based on abyssal peridotite isotopic compositions. J. Geophys. Res. 114, B12203. https://doi.org/10.1029/2008JB006186.

Warren, J.M., 2016. Global variations in abyssal peridotite compositions. Lithos 248–251, 193–219. https://doi.org/10.1016/j.lithos.2015.12.023.

Wells, P.R.A., 1977. Pyroxene thermometry in simple and complex systems. Contrib. Mineral. Petrol. 62, 129–139. https://doi.org/10.1007/BF00372872.

Wilke, M., Behrens, H., Burkhard, D.J.M., Rossano, S., 2002. The oxidation state of iron in silicic melt at 500 MPa water pressure. Chem. Geol. 189, 55–67.

Witt-Eickschen, G., O'Neill, H.S.C., 2005. The effect of temperature on the equilibrium distribution of trace elements between clinopyroxene, orthopyroxene, olivine and spinel in upper mantle peridotite. Chem. Geol. 221, 65–101. https://doi.org/10.1016/j.chemgeo.2005.04.005.

Wood, B.J., 1990. An experimental test of the spinel peridotite oxygen barometer. J. Geophys. Res. 95, 15845–15851. https://doi.org/10.1029/JB095iB10p15845.

Wood, B.J., Bryndzia, L.T., Johnson, K.E., 1990. Mantle oxidation state and its relationship to tectonic environment and fluid speciation. Science 248, 337–345. https://doi.org/10.1126/science.248.4953.337.

Wood, B.J., Virgo, D., 1989. Upper mantle oxidation state: ferric iron contents of lherzolite spinels by ^{57}Fe Mössbauer spectroscopy and resultant oxygen fugacities. Geochim. Cosmochim. Acta 53, 1277–1291. https://doi.org/10.1016/0016-7037(89)90062-8.

Woodland, A.B., Kornprobst, J., McPherson, E., Bodinier, J.-L., Menzies, M.A., 1996. Metasomatic interactions in the lithospheric mantle: petrologic evidence from the Lherz massif, French Pyrenees. Chem. Geol. 134, 83–112.

Zhang, H.L., Cottrell, E., Solheid, P., Kelley, K.A., Hirschmann, M.M., 2018. Determination of $Fe^{3+}/\Sigma Fe$ of XANES basaltic glass standards by Mössbauer spectroscopy and its application to the oxidation state of iron in MORB. Chem. Geol. 479, 166–175. https://doi.org/10.1016/j.chemgeo.2018.01.006.